



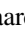






# The NuSTAR, XMM-Newton, and Suzaku View of A3395 at the Intercluster Filament Interface

Ayşegül Tümer<sup>1</sup> , Daniel R. Wik<sup>1</sup> , Massimo Gaspari<sup>2,3</sup> , Hiroki Akamatsu<sup>4</sup> , Niels J. Westergaard<sup>5</sup> ,  
Francesco Tombesi<sup>6,7,8,9</sup> , and E. Nihal Ercan<sup>10</sup> 

<sup>1</sup> Department of Physics & Astronomy, University of Utah, 115 South 1400 East, Salt Lake City, UT 84112, USA; [aysegultumer@gmail.com](mailto:aysegultumer@gmail.com)

<sup>2</sup> INAF, Osservatorio di Astrofisica e Scienza dello Spazio, via Pietro Gobetti 93/3, I-40129 Bologna, Italy

<sup>3</sup> Department of Astrophysical Sciences, Princeton University, 4 Ivy Lane, Princeton, NJ 08544-1001, USA

<sup>4</sup> SRON Netherlands Institute for Space Research, Niels Bohrweg 4, 2333 CA Leiden, The Netherlands

<sup>5</sup> DTU Space, Technical University of Denmark, Elektrovej Building 327, DK-2800 Kgs Lyngby, Denmark

<sup>6</sup> Department of Physics, University of Rome “Tor Vergata”, Via della Ricerca Scientifica 1, I-00133 Rome, Italy

<sup>7</sup> Department of Astronomy, University of Maryland, College Park, MD 20742, USA

<sup>8</sup> NASA/Goddard Space Flight Center, Code 662, Greenbelt, MD 20771, USA

<sup>9</sup> INAF Osservatorio Astronomico di Roma, Via Frascati 33, I-00078 Monteporzio Catone, Italy

<sup>10</sup> Department of Physics, Boğaziçi University, Bebek, 34342 Istanbul, Turkey

Received 2021 December 10; revised 2022 February 28; accepted 2022 March 27; published 2022 May 5

## Abstract

Galaxy clusters are the largest virialized objects in the universe. Their merger dynamics and their interactions with the cosmic filaments that connect them are important for our understanding of the formation of large-scale structure. In addition, cosmic filaments are thought to possess the missing baryons in the universe. Studying the interaction of galaxy clusters and filaments therefore has the potential to unveil the origin of the baryons and the physical processes that occur during merger stages of galaxy clusters. In this paper, we study the connection between A3395 and the intercluster filament with NuSTAR, XMM-Newton, and Suzaku data. Since the NuSTAR observation is moderately contaminated by scattered light, we present a novel technique developed for disentangling this background from the emission from the intracluster medium. We find that the interface of the cluster and the intercluster filament connecting A3395 and A3391 does not show any signs of heated plasma, as was previously thought. This interface has low temperature, high density, and low entropy, thus we suggest that the gas is cooling, being enhanced by the turbulent or tidal “weather” driven during the early stage of the merger. Furthermore, our temperature results from the NuSTAR data are in agreement with those from XMM-Newton and from joint NuSTAR and XMM-Newton analysis for a region with  $\sim 25\%$  scattered light contamination within  $1\sigma$ . We show that the temperature constraint of the intracluster medium is valid even when the data are contaminated up to  $\sim 25\%$  for  $\sim 5$  keV cluster emission.

*Unified Astronomy Thesaurus concepts:* [Galaxy clusters \(584\)](#); [Intracluster medium \(858\)](#); [High energy astrophysics \(739\)](#); [Cosmic web \(330\)](#); [Large-scale structure of the universe \(902\)](#)

## 1. Introduction

Clusters of galaxies are the largest gravitationally bound structures in the universe. Elements produced inside a galaxy cluster can rarely escape its deep gravitational potential well; therefore these constituents make clusters great probes for understanding the evolutionary history of large-scale structures. The intracluster medium (ICM) is an optically thin hot plasma ( $\sim 10^7$ – $10^8$  K) that fills the volume between cluster galaxies. It accounts for  $\sim 12\%$  of the total matter inside galaxy clusters and its emission prevails in the X-ray band of the electromagnetic spectrum (see, e.g., Sarazin 1986). X-ray-emitting processes in the ICM are mainly in the form of thermal bremsstrahlung and line emission. The plasma is close to hydrostatic equilibrium in relaxed clusters with a smooth, centrally peaked X-ray surface brightness distribution. However, a significant number of clusters show multi-peaked brightness distributions, pointing to multiple substructures that indicate ongoing merger activity (Nakamura et al. 1995).

According to scenarios for the formation of large-scale structure, clusters of galaxies are hierarchically formed by the merger of smaller-scale structures. The collisions of these substructures happen at very high velocities ( $\sim 2000$  km s $^{-1}$ ) and the energy released is of the order of  $10^{65}$  erg, making them the second most energetic events in the universe, following the Big Bang. This energy mostly is dissipated into the ICM through the creation of turbulence, magnetic fields, and relativistic particles (e.g., Markevitch et al. 1999; Gaspari & Churazov 2013), and it is ultimately thermalized.

Major mergers between clusters of comparable masses produce giant shock waves that can be directly detected in the density and temperature structure of the gas, and both major and minor mergers can disturb the cool gas at cluster centers, causing it to “slosh” and produce cold fronts (see, e.g., Markevitch & Vikhlinin 2007, for a review). Shock heating is indirectly evidenced by high entropy regions inside clusters (see, e.g., Henry & Briel 1995), and shock fronts create sharp surface brightness discontinuities along with temperature jumps characterized by a Mach number  $\lesssim 3$  (Markevitch & Vikhlinin 2007). The boundary between a cluster and the intergalactic medium is defined by an accretion shock, where cooler gas meets the hotter gas of the ICM, which lies beyond the virial radius. In contrast, filaments can penetrate more



Original content from this work may be used under the terms of the [Creative Commons Attribution 4.0 licence](#). Any further distribution of this work must maintain attribution to the author(s) and the title of the work, journal citation and DOI.

deeply into clusters, potentially creating shocks in locations where the gas is more easily observable in X-rays (e.g., Zinger et al. 2016).

The existence of substructures in clusters of galaxies, since dynamical evolution is prone to wipe them out, points to dynamically young systems, i.e., clusters at a pre-merger stage (Flin 2003). Thermodynamical properties of the X-ray-emitting ICM are sensitive probes of these dynamical activities; moreover, in conjunction with the coevolving central supermassive black holes, such processes are key to shaping ICM X-ray scaling relations (Gaspari et al. 2019; Lovisari et al. 2021).

Clusters of galaxies are not completely isolated structures but are connected to the web-like structure of the matter distribution in the universe. This cosmic web consists of sheets, filaments, knots, and voids, where galaxies form and evolve (Bond et al. 1996). About  $\sim 50\%$  of the baryonic matter lies in filaments, which only constitute  $\sim 6\%$  of the volume (Cautun et al. 2014), making filaments relatively high-density structures, and galaxy clusters are found where they intersect. They are the end product of gravitational collapse of matter, where the baryonic gas follows the dark matter distribution (see, e.g., Hahn et al. 2007; Codis et al. 2012; Laigle et al. 2015; Kraljic et al. 2018) that grew from small overdensities in the early universe. Clusters of galaxies sit in the highest-density regions of this web, making cluster outskirts an inherently interesting region for the understanding of the formation, evolution, and cosmology of large-scale structures (Kuchner et al. 2020).

At a redshift  $z=0.0498$ , Abell 3395 (hereafter A3395) extends out to a virial radius  $r_{180}=34.6$  (Markevitch et al. 1998) and is classified as a merging clusters of galaxies, with its subclusters estimated to be near their first core passage (Lakhchaura et al. 2011). These subclusters are found to be close in redshift, indicating that the merger is taking place in the plane of the sky. However, the structure of the cluster seems to be even more complex, with two more relatively strong surface brightness peaks between the subclusters and an additional surface brightness excess to the west (Lakhchaura et al. 2011). Two scenarios are proposed for the origin of the surface brightness peaks in these regions by Lakhchaura et al. (2011). The first scenario considers the western (W) subclump being a separate system that is in the first stage of a merger and falling into the common gravitational potential of the northeastern (NE) and southwestern (SW) subclusters. This scenario unfortunately does not explain the existence of the bridge (B) structure between the NE and SW subclusters. Another possibility is that we are witnessing the aftermath of a merger between the subclusters that has already occurred, with the bridge and W subclump resulting from ram pressure stripping of gas from the SW subcluster, possibly in two different phases. Moreover, the lack of prominent cool cores at the centers of the NE and SW subclusters is particularly interesting if these structures have not yet gone through a merger, since mergers are assumed to be the main processes that disrupt cool cores, given that feedback by central active galactic nuclei (AGNs) is expected to be self-regulated and gentle (Gaspari et al. 2020). In addition, diffuse radio structures lying in the W subclump have recently been discovered (Reiprich et al. 2021).

In addition, the cluster is part of a larger network of clusters and groups, where an emission bridge connecting A3395 to Abell 3391 (hereafter A3391) has also been discovered along with a group of galaxies lying in between A3395 and A3391

(Tittley & Henriksen 2001; Planck Collaboration et al. 2013; Sugawara et al. 2017; Alvarez et al. 2018). In this work, we refer to this emission bridge as “the intercluster filament.” The intercluster filament has also recently been confirmed and studied in detail with eROSITA (Reiprich et al. 2021). Furthermore, this network has been mapped by Chandra and through the thermal Sunyaev–Zel’dovich (SZ) effect using the Planck High Frequency Instrument by Bourdin et al. (2020), which clearly shows the intercluster filament connected to the ICM of both clusters. These clusters are thought to have already begun interacting via this filament and might be at a pre-merger stage (Sugawara et al. 2017).

The excess emission is thought to originate from the interaction of A3395 and A3391, which resulted in tidally stripped cluster gas because of the lack of detection of warm ( $kT < 1$  keV) gas (Sugawara et al. 2017; Alvarez et al. 2018). This intercluster filament emission, which extends up to 3 Mpc, could not be fully explained by the galaxy group emission alone, but hints at the existence of warm and primordial filamentary gas.

Alvarez et al. (2018) suggest that the intercluster filament region is filled with tidally removed ICM from A3395 and A3391, evidenced by the filament temperature and entropy, which suggests a pre-merger stage. They also state that, although the global temperature ( $kT = 4.45_{-0.55}^{+0.89}$  keV) and entropy profiles are higher than what is expected for the warm-hot intergalactic medium (WHIM) at this redshift (Valageas et al. 2003), the density ( $n_e = 1.08_{-0.05}^{+0.06} \times 10^{-4}$  cm $^{-3}$ ) of the filament is in agreement with the WHIM, as are the cluster outskirts.

Also, a hot spot ( $kT \simeq 9$  keV) was detected with XMM-Newton in the NW region of A3395 by Lakhchaura et al. (2011), and they suggest that this region of the cluster is part of the intercluster filament.

The A399–A401 system has the other Planck-detected filament (Planck Collaboration et al. 2013). Bonjean et al. (2018) favor the scenario in which the emission bridge between A399 and A401 is associated with a cosmic filament, where the gas is collapsing and being heated by the future merger of these clusters. Akamatsu et al. (2017) and Hincks et al. (2022) discuss the effects of projection on the temperature and density estimations. Other similar galaxy cluster pre-mergers with an intercluster filament are seen in the A21-PSZ2 G114.90–34.35 pair (Bonjean et al. 2018), the Shapley supercluster (connecting A3562, A3558, and A3556 (Kull & Böhringer 1999), and the A222–A223 pair (Werner et al. 2008). The Shapley supercluster was observed with ROSAT. The authors debate that the origin of the excess emission is either overlapping gas distributions of A3558 and A3556 or an intrasupercluster emission (Kull & Böhringer 1999). Werner et al. (2008) claim that the emission bridge connecting A222 and A223 is the hottest and densest phase of the WHIM, due to the temperature and average density of the observed gas.

Our main objective in this work is to understand the ICM and intercluster filament interaction at the junction of the cluster outskirts and the intercluster filament, which is different from the aforementioned studies that focus on the emission bridges. To achieve this, high-precision temperature measurement of this region is required to assess possible heating at the site. The peak effective area of NuSTAR (the Nuclear Spectroscopic Telescope Array; Harrison et al. 2013) at  $E \sim 10$  keV and its 3–79 keV operating energy band enables

the detection of recently shocked gas. Given that the hot spot seems to be at a temperature  $\sim 9$  keV (Lakhchaura et al. 2011), NuSTAR is the only observatory that is capable of making the measurement with highest precision required.

In this paper, we present results from the analysis of NuSTAR, XMM-Newton, and Suzaku data to study the interaction of A3395 outskirts with the intercluster filament that connects A3395 and A3391.

The paper is organized as follows: observations, the data reduction process, and the background assessment of the NuSTAR, XMM-Newton, and Suzaku data are presented in Section 2. In Section 3, methods used for the analysis of the cluster are described, including our technique to treat the scattered light, and we present our results. We then discuss our findings in Section 4 and conclude our work in Section 5.

Throughout this paper, we assume the  $\Lambda$ CDM cosmology with  $H_0 = 70$  km s<sup>-1</sup> Mpc<sup>-1</sup>,  $\Omega_M = 0.3$ , and  $\Omega_\Lambda = 0.7$ . According to these assumptions, a projected intracluster distance of 100 kpc corresponds to an angular separation of  $\sim 103''$  at the redshift of A3395, which makes the conversion from angular distance to physical distance straightforward for studying the images. The redshift value is fixed at  $z = 0.0498$  (SIMBAD<sup>11</sup> astronomical database), and we adopt a neutral hydrogen column density of  $N_H = 6.30 \times 10^{20}$  cm<sup>-2</sup> based on the Leiden/Argentine/Bonn Galactic H I survey (Kalberla et al. 2005). We used the abundance table of Anders & Grevesse (1989) for XMM-Newton since the XMM-Newton analyses in the literature were made using older tables. For Suzaku analysis, we used protosolar abundances (Lodders et al. 2009). For NuSTAR and joint NuSTAR and XMM-Newton analyses, we used the abundance table of Wilms et al. (2000). For the spectral analysis of NuSTAR data as well as for the joint fitting procedure of NuSTAR and XMM-Newton data, photon counts used in spectra are grouped to have at least three counts per bin; therefore we do not apply the  $\chi^2$  statistics, which requires a minimum of  $\sim 25$  counts in each energy bin. Since the data follow a Poisson distribution, we applied the maximum likelihood-based statistic (hereafter, C-stat) appropriate for Poisson data as proposed by Cash (1979). However, with XMM-Newton and Suzaku analyses, photon counts used in spectra are grouped to have at least 25 counts in each bin, and we used  $\chi^2$  statistics to minimize differences in grouping and statistical approach with the literature. All uncertainties are quoted at the 68% confidence level unless otherwise stated.

## 2. Observations and Data Reduction

In this work, we utilize NuSTAR, XMM-Newton, and Suzaku data to study the interface of A3395 and the intercluster filament that connects A3395 to A3391. The field of view (FOV) of the observations that are used in this work is overlaid on the recent eROSITA events binned by  $128 \times 128$  as shown in Figure 1. We retrieved the eROSITA data from the Early Data Release observations with Obs.ID 300014.<sup>12</sup> The data from XMM-Newton and Suzaku are retrieved from HEASARC archives.<sup>13</sup> whereas the NuSTAR data were privately communicated to our group by the NuSTAR SOC team as part of the NuSTAR guest observer (Cycle-6) program award with an exclusive use period of one year. The public release date for the

data was 2021-09-21. The specifications of the data are summarized in Table 1.

### 2.1. NuSTAR

NuSTAR observed the northwestern region of A3395 at the junction of cluster and intercluster filament (Figure 1) for  $\sim 130$  ks during 2020 with the focal plane modules (FPMA and FPMB) with an offset pointing from the central cluster emission (Table 1).

In order to filter the data, standard pipeline processing is carried out using HEASoft (v. 6.28) and NuSTARDAS (v. 2.0.0) tools. Since the NuSTAR observation of A3395 was performed after 2020 March 16, the use of versions of HEASoft earlier than v. 6.27.1 and of NuSTARDAS earlier than v. 1.9.2 results in errors during pipeline processing.<sup>14</sup> To clean the event files, stages 1 and 2 of the NuSTARDAS pipeline processing script nupipeline are used. Regarding the cleaning of the event files for the passages through the South Atlantic Anomaly (SAA) and a tentacle-like region of higher activity near part of the SAA, instead of using SAAMODE = STRICT and TENTACLE = yes calls, we have created light curves and applied different filters to create good time intervals (GTIs) manually without fully discarding the passage intervals.

The new set of GTIs are reprocessed with nupipeline stages 1 and 2, and images are generated at different energy bands with XSELECT. nuexpomap is used to create exposure maps. To produce the corresponding spectra for the regions of interest as well as the corresponding response matrix files (RMFs) and ancillary response files (ARFs), stage 3 of nupipeline is used.

The background assessment of NuSTAR is particularly challenging due to the open mast between the focal plane modules and the optics assembly. The main components of the background are instrument Compton-scattered continuum emission, instrument activation and emission lines, cosmic X-ray background from the sky leaking past the aperture stops, reflected solar X-rays, and focused and ghost-ray cosmic X-ray background. Modeling the background where there is a lack of cluster emission regions is tricky since the ICM emission becomes an additional component in the background fitting procedure.

To apply these models for the cluster background assessment, a set of IDL routines called nuskybgd, which defines the background spatially and spectrally, is utilized (Wik et al. 2014). The procedure starts by selecting regions in the FOV where the cluster emission is inherently present yet not the most dominant. To account for the ICM emission, an apec model is included in the full set of models, and jointly fitted with the background (Figure 12 in Appendix A). The global background model is used to create background images, which are then subtracted from the cleaned images and corrected by the corresponding exposure maps. Background-subtracted, exposure-corrected images at different energy bands are presented in Figure 2.

Once the background is defined for any region in the FOV both spatially and spectrally, the next steps are to select regions of interest, to extract spectra and the corresponding files, and to

<sup>11</sup> <http://simbad.u-strasbg.fr/simbad/>

<sup>12</sup> <https://erosita.mpe.mpg.de/edr/eROSITAobservations/>

<sup>13</sup> <https://heasarc.gsfc.nasa.gov/cgi-bin/W3Browse/w3browse.pl>

<sup>14</sup> [http://nustarsoc.caltech.edu/NuSTAR\\_Public/NuSTAROperationSite/software\\_calibration.php/](http://nustarsoc.caltech.edu/NuSTAR_Public/NuSTAROperationSite/software_calibration.php/)



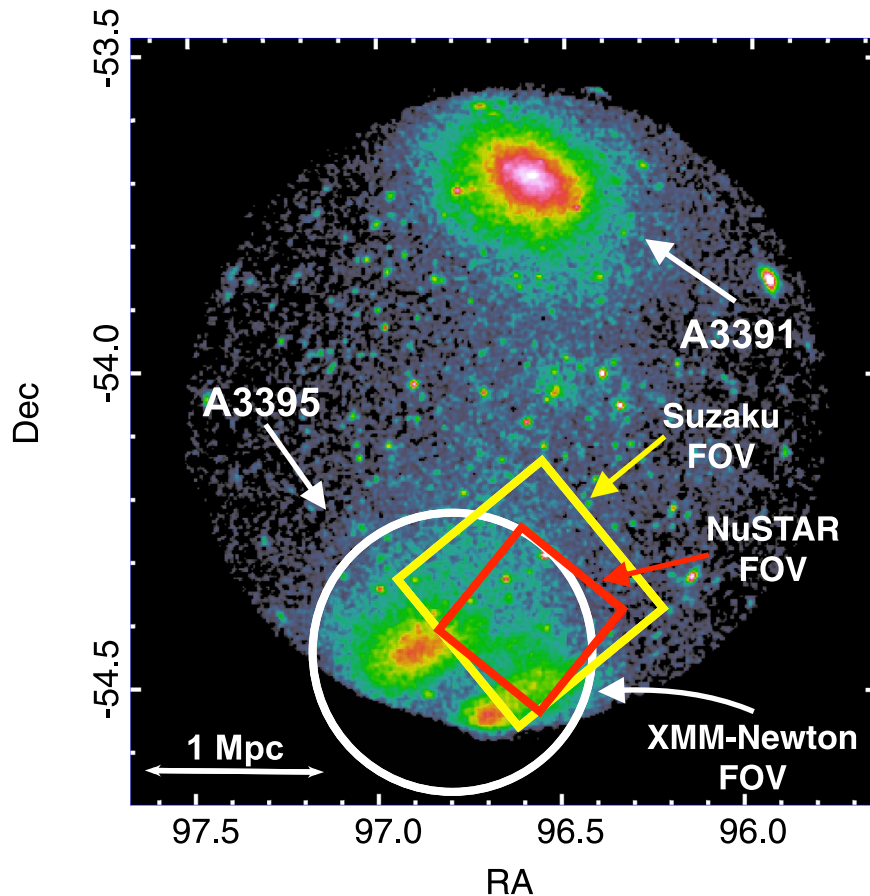


**Figure 1.** eROSITA image of the A3395 and A3391 system. NuSTAR, XMM-Newton, and Suzaku FOVs are indicated with a red box, white circle, and yellow box, respectively.

generate the specific background model, followed by spectral fitting to evaluate the physical properties of the ICM.

## 2.2. XMM-Newton

XMM-Newton observations lasted for  $\sim 30$  ks during 2007 (Table 1). The FOV of this observation is focused on the central region of A3395, which extends to  $\sim r_{500}$  (Figure 1). The three EPIC cameras MOS1, MOS2 (Turner et al. 2001), and PN (Strüder et al. 2001) were operated in full frame mode with the Thin1 filter.

We used standard procedures from the Science Analysis System (SAS) software version 16.1.0, along with the Extended Source Analysis Software (ESAS<sup>15</sup>) package. Calibrated photon event files were produced using the epcchain and emchain tasks. For obtaining the GTIs, we used mos-filter and pn-filter tasks. Point sources were detected by the cheese routine.

ESAS routines mos\_back and pn\_back embedded in SAS create model quiescent particle background (QPB) spectra and images for selected regions from the intermediate files produced from the mos spectra and pn spectra. To create background-subtracted, exposure-corrected images, first a spectrum for the source and the QPB was extracted from the full FOV. This spectrum was fitted with the absorbed apec model for the cluster emission plus the models for the background. The background model components are the

cosmic diffuse X-ray background (CXB), solar wind charge exchange (SWCX), and particle and residual soft proton contamination ( $K\alpha$  SP).

CXB is modeled with an unabsorbed thermal component of about 0.1 keV, an absorbed thermal component of about 0.25 keV, and the extragalactic power law with a spectral index of 1.46. The particle background is Gaussian lines at 1.496 and 1.75 keV representing the Al  $K\alpha$  and Si  $K\alpha$  lines in the MOS, lines at 1.496 keV and near 8 keV representing the Al  $K\alpha$  and Cu fluorescent lines in the PN. Possible SWCX produces two more lines at 0.56 and 0.65 keV, and the residual SP is represented by a broken power law and fitted with a diagonal matrix supplied in the XMM-ESAS CalDB release, mos1-diag.rsp.gz, mos2-diag.rsp.gz, and pn-diag.rsp.gz.  $K\alpha$  proton\_scale was used as a constant model between the cameras in the fit model to find the solid angle on each detector for the fit. The routine proton takes the fitted parameters from the fit of the SP model, then creates SP background images later to be subtracted as a background from the photon image.

This process is repeated for an annulus selected in an outer region of the FOV to exclude the bright cluster emission at the center of the FOV in order to produce a better fit for the SP contamination. The resulting SP normalization from the annulus fit is then renormalized to the full FOV using proton\_scale. The resulting adaptively smoothed, background-subtracted, exposure-corrected images are obtained with tasks comb and adapt, as shown in Figure 3.

In addition to the ESAS background, the total background model used to fit the spectra contains the following

<sup>15</sup> <https://heasarc.gsfc.nasa.gov/docs/xmm/esas/cookbook/xmm-esas.html>

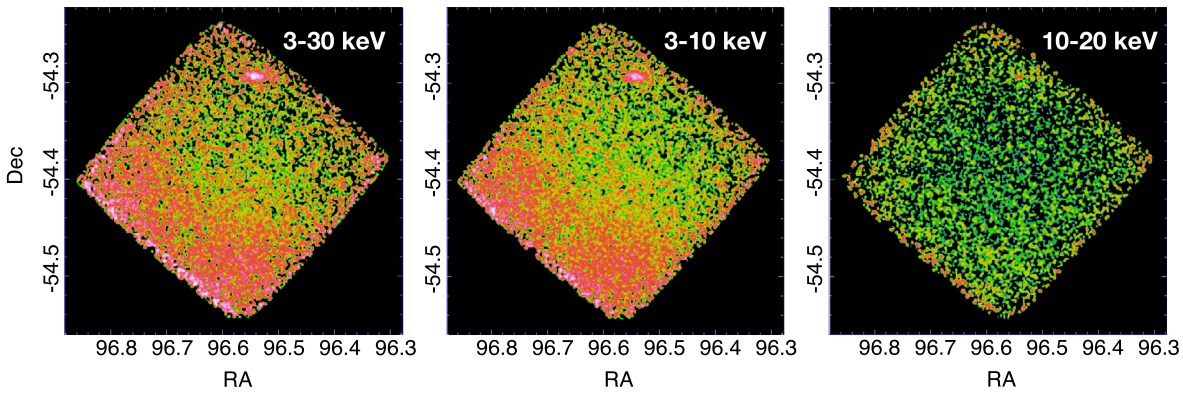


**Figure 2.** NuSTAR background-subtracted, exposure-corrected, smoothed photon images of A3395 at various energy bands.

**Table 1**  
Observation Log

Telescope	Observation ID	Start Date (YYYY-mm-dd)	PI	Equatorial Coordinates (J2000)	Total Effective Exposure Time (ks) <sup>a</sup>
NuSTAR	70601003002	2020-09-09	A. Tümer	06:26:22, -54:23:47	250.4 (97.4%)
XMM-Newton	0400010301	2007-01-24	M. Henriksen	06:27:11, -54:27:59	78.9 (90.4%)
Suzaku	807031010	2013-02-06	N. Tanaka	06:26:26, -54:20:22	100.5 (82.5%)

**Note.**

<sup>a</sup> Combined instrument exposures, i.e., FPMA and FPMB for NuSTAR; MOS1, MOS2, and PN for XMM-Newton; and XIS1, XIS2, and XIS3 for Suzaku. Percentages correspond to the accepted data after filtering, with respect to the total raw exposure time.

components: Gaussian + Gaussian + Gaussian + Gaussian + Gaussian + Gaussian + Gaussian + constant  $\times$  constant  $\times$  (Gaussian + Gaussian + apec + (apec + apec + powerlaw  $\times$  wabs), where the second constant corresponds to the cross-calibration of instruments MOS1, MOS2, and PN. This background modeling is used for the rest of the spectral analysis in this paper.

### 2.3. Suzaku

Suzaku (Mitsuda et al. 2007) also covered a region enclosing the NuSTAR FOV (Figure 1) for  $\sim 47$  ks in 2013. The X-ray Imaging Spectrometer (XIS; Koyama et al. 2007) of Suzaku is one of the best instruments to investigate shallow cluster emission in the outskirts owing to their low and stable background. The basic data analysis and results are presented in Sugawara et al. (2017). Here we briefly explain the data reduction and spectral analysis approach.

We followed the approach presented in Sugawara et al. (2017). We used the latest calibration file (20160607) and performed event screening with cutoff rigidity greater than 8 GV. The area damaged by micrometeoroids in the XIS0 instrument was excluded in the following analysis (<http://www.astro.isas.jaxa.jp/suzaku/doc/suzakumemo/suzakumemo-2010-01.pdf>). An additional screening is applied for XIS1 to mitigate the increase in non-X-ray background (NXB) due to an increase in the amount of charge injection ([http://www.astro.isas.jaxa.jp/suzaku/analysis/xis/xis1\\_ci\\_6\\_nxb](http://www.astro.isas.jaxa.jp/suzaku/analysis/xis/xis1_ci_6_nxb)). The cleaned exposure time is about 33 ks for each instrument. In order to characterize the ICM emission, all background components need to be constrained well. For the estimation of the NXB, we used a database constructed from observations of Earth at night using the ftool `xisnxbgen` (Tawa et al. 2008). For the sky background consisting of cosmic-ray background, local hot

bubble, and Milky Way halo, we used model presented in Table 2 of Sugawara et al. (2017).

RMFs and ARFs are generated by the ftools `xisrmfgen` and `xissimarfgen` (Ishisaki et al. 2007). For the ARFs, we assumed uniform emission from a circular region with  $20'$  radius as an input image. Throughout the fitting procedure, the normalization between back-illuminated (BI) and front-illuminated (FI) instruments is kept free.

## 3. Data Analysis and Results

### 3.1. Global View

We start the analysis with the characterization of the global emission at the NuSTAR FOV that is pointed at the northwestern region of A3395. We selected a square  $12' \times 12'$  region from which we extracted a spectrum and applied a single-temperature `apec` model (Smith et al. 2001) using `XSPEC` (v. 12.11.1; Arnaud 1996). Since NuSTAR is not sensitive to emission below 3 keV, it is also not affected by foreground absorption by the Galactic hydrogen column density, and any changes in the  $N_{\text{H}}$  value do not affect the thermodynamical values obtained from the fit. We visually inspected the images for the point sources, and excluded a  $1'$  (comparable to the half-power diameter of NuSTAR's point-spread function) circular region from the location of the point source that is visible in Figure 2.

The spectral fit and the corresponding values are presented in Figure 4 and Table 2, respectively. It is evident from the spectra and the C-stat values that a single-temperature plasma does not fully describe the cluster. This is expected since the NuSTAR observation is pointed at a region where there are multiple substructures, which may involve emission features from different sources. To assess the possibility of multiple temperatures, we have added another `apec` model for a

**Table 2**  
Spectral Parameters of NuSTAR for the Global Analysis

	$kT$ (keV)	$Z$ ( $Z_{\odot}$ )	$norm$ ( $10^{-2} \text{ cm}^{-5}$ )	$\Gamma$	$\kappa$ ( $10^{-3}$ )	$C/\nu$ C-stat/d.o.f.
apec	$5.59 \pm 0.11$	$0.05 \pm 0.02$	$1.42 \pm 0.03$	...	...	1219.22/844
apec + powerlaw	$2.06^{+0.31}_{-0.22}$	$0.36^{+0.16}_{-0.11}$	$2.13^{+0.19}_{-0.23}$	$1.82^{+0.18}_{-0.29}$	$1.75^{+1.04}_{-0.95}$	902.55/842

**Note.** apec normalization ( $norm$ ) is given by  $\frac{10^{-14}}{4\pi[D_A(1+z)]^2} \int n_e n_H dV$  where powerlaw normalization ( $\kappa$ ) is photons  $\text{keV}^{-1} \text{ cm}^{-2} \text{ s}^{-1}$  at 1 keV. All errors are quoted at 68% confidence level.

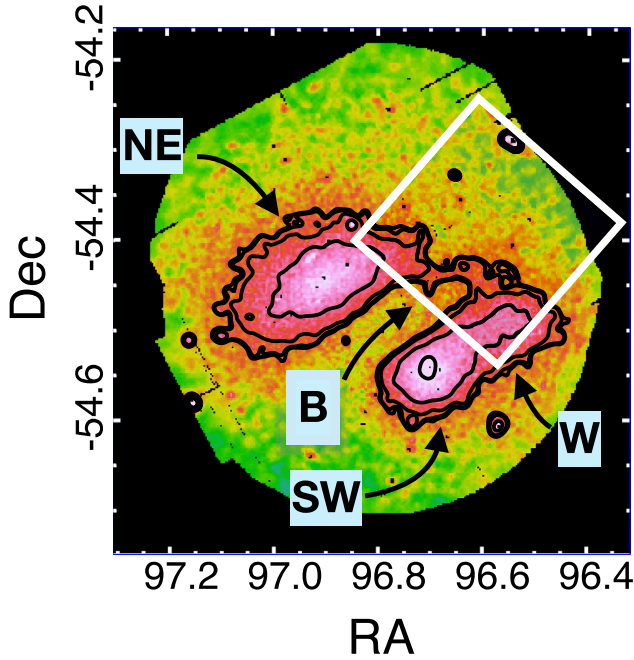


**Figure 3.** Background-subtracted, exposure-corrected, adaptively smoothed XMM-Newton photon image in the soft X-ray (0.4–2.5 keV) band. The NuSTAR field of view is indicated by the white box. NE and SW are subclusters of A3395, B indicates the bridge emission between the subclusters, and W indicates the western subclump as described in Section 1.

secondary temperature structure, yet the higher-temperature component was not constrained.

One of these emission features can also be due to a nonthermal component, namely inverse Compton (IC) scattering, which is well represented by a power-law distribution and corresponds to the model `powerlaw` in XSPEC. The addition of a `powerlaw` model to the original `apec` seems to describe the overall cluster emission well, but the reason for this extra component may be completely unrelated to cluster physics, namely scattered light caused by the two main subclusters lying just outside the FOV. This additional component also seems to suppress the ICM to an unrealistic low temperature with respect to what is found in the literature (Markevitch et al. 1998; Lakhchaura et al. 2011; Alvarez et al. 2018), further suggesting a scattered light origin.

### 3.2. $6 \times 6$ Grid Analysis

Since A3395 has many substructures within the NuSTAR FOV, a typical assumption of spherical symmetry cannot be used for region selection. For the characterization of the regions, we have created thermodynamical maps of a  $12' \times 12'$  square region, encompassing a  $6 \times 6$  grid system as shown in

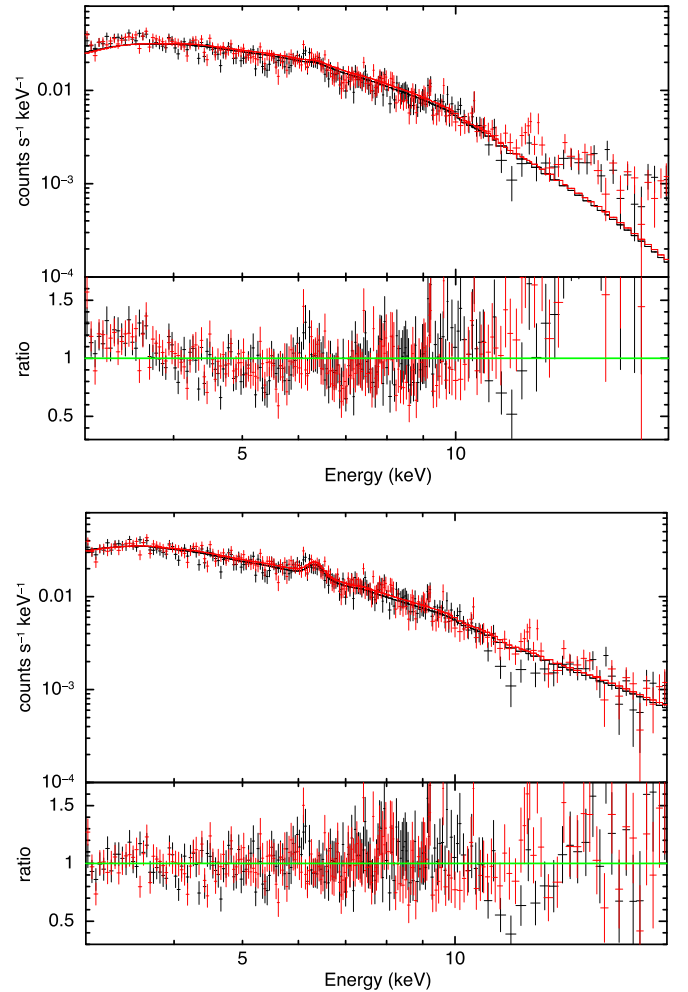


**Figure 4.** Global fits with single `apec` (upper panel) and `apec + powerlaw` (lower panel) of the  $12' \times 12'$  region.

Figure 5. This method is used to aid our understanding of the cluster ICM in detail, as done by Gastaldello et al. (2015) for the NuSTAR observation of the Coma cluster. We use these results to select regions with similar thermodynamical properties to define larger regions with higher signal-to-noise ratio (S/N).

For this analysis, we calculated projected maps, since the main goal is to achieve a comparative study, rather than to study the specific density, entropy, and pressure properties. To assess the ICM properties of box 7, we excluded the point source in that region. Although there will also be scattered light contamination in these regions, we expect the scattered light to change mildly in the adjacent regions due to the small region



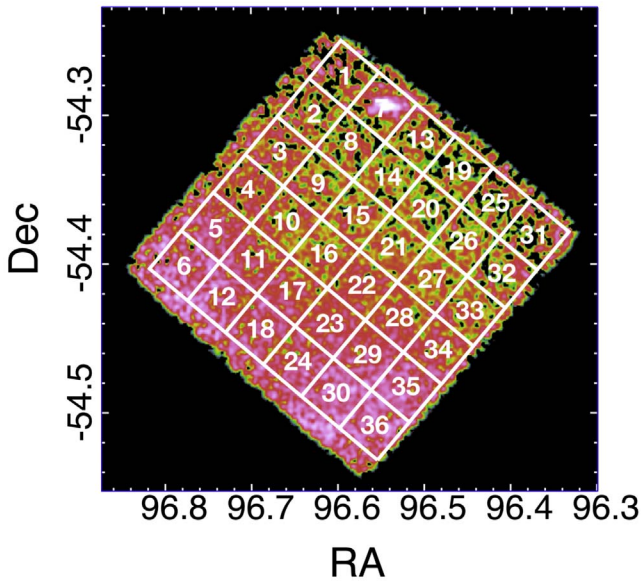


**Figure 5.** Grid system and region numbers superimposed on background-subtracted, exposure-corrected NuSTAR photon images of A3395 in the 3–20 keV energy band. The spectrum of each region is fitted with a single-temperature model to build the thermodynamical profiles.

size we select. This means that, even if a most complete assessment of ICM properties may not be managed, we aim to still have a good proxy for the definition of regions of interest.

The grid system analysis is achieved with NuSTAR data, where we extracted spectra from each grid then fitted them using a single-temperature `apec` model. The abundances for the fits are fixed to  $Z = 0.3 Z_{\odot}$ , because they were difficult to constrain due to low S/N. For the selection of regions with similar thermodynamical properties for the whole FOV, maps of NuSTAR temperature, density, entropy, and pressure were created. The normalization of the `XSPEC` model `apec` is defined as  $[10^{-14}/4\pi[D_A(1+z)]^2] \int n_e n_H dV$ , where the integrand is the emission measure (EM),  $n_e$  and  $n_H$  are electron and hydrogen densities in  $\text{cm}^{-3}$ , and the angular diameter distance to A3395 is  $D_A \simeq 6.20 \times 10^{26}$  cm. By using the normalization of the `apec` model, we estimated the EM, and the corresponding pseudo-pressure and pseudo-entropy maps using  $P = kT \times \text{EM}^{1/2}$  and  $S = kT/\text{EM}^{1/3}$  (e.g., Rossetti et al. 2007). The projected density is calculated as the square root of the normalization parameter of the `apec` model.

Following the results of our grid analysis and with the guidance of the XMM-Newton photon image, we defined six regions of interest on the NuSTAR FOV (Figure 7). Region A represents the location of the hot spot detected by XMM-Newton (Lakhchaura et al. 2011), Region B is the region extending to the intercluster filament, Region E is the bridge between the subclusters of A3395, and Region F is the tail of the southwestern subcluster (or the W clump). Region C is isolated since it shows higher-density regions than Regions A and B from our NuSTAR grid analysis (Figure 6), and also shows excess emission in the eROSITA image, probably of filamentary origin (Figures 1 and 7, middle panel). We note that Regions A, B, and C are mostly enclosed in the region isolated by Lakhchaura et al. (2011) (indicated by NW), which they suggest connects the cluster to the intercluster filament.

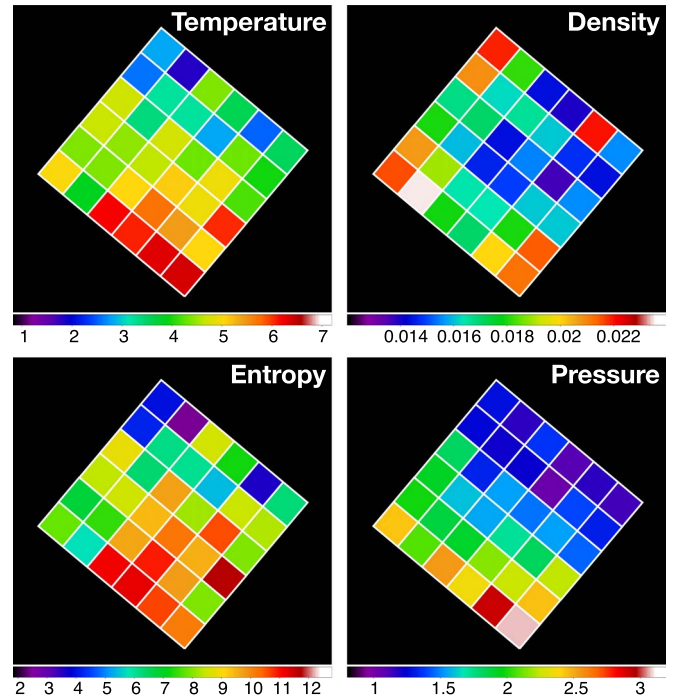


**Figure 6.** Projected maps of NuSTAR temperature (upper left), projected density (upper right), pseudo-entropy (lower left), and pseudo-pressure (lower right). Temperature is given in units of keV, whereas the other maps are presented in arbitrary units and do not account for the possible scattered light contamination.

### 3.3. Scattered Light and Ray-trace Simulations

NuSTAR is affected by scattered light contamination (also known as Ghost Rays; Madsen et al. 2017) due to X-ray photons that undergo only a single reflection off either the primary (upper) or secondary (lower) mirror, as opposed to a properly focused double reflection. Due to the lack of precollimators, photons from bright sources outside the FOV can reach the focal plane without double reflection.

The upper single reflection is due to the photons that strike the upper mirrors at angles steeper than the nominal focusing graze angle; it fades away when the angle becomes too steep so that the adjacent shell shadows it (Madsen et al. 2017). The aperture stop also helps to block some of these photons. The lower single reflection, on the other hand, is caused by photons reaching the mirrors at angles that are shallower than the nominal graze angle (Madsen et al. 2017). In addition, back reflections can occur, in which photons hit the back side of the upper mirror of the adjacent shell first, then reflect off the front side of the mirror shell. The scattered light contamination appears as early as  $2'$  off-axis but only becomes significant above  $3'$ , out to  $\sim 1^\circ$  (Madsen et al. 2017). The off-axis and energy dependence of scattered light is understood for point sources (Madsen et al. 2017), but no data analysis tool yet exists to model its effect in the case of extended emission. Ray-trace simulators, which trace out the paths of photons through the optics and onto the detectors, have been shown to reproduce observed scattered light patterns (Westergaard 2011; Madsen et al. 2017).

We analyzed the effect of the scattered light for the NuSTAR observation, in an attempt to explain the excess power-law emission in the global spectra. Also, this is already expected since the two main subclusters, namely NE and SW (Figure 7),

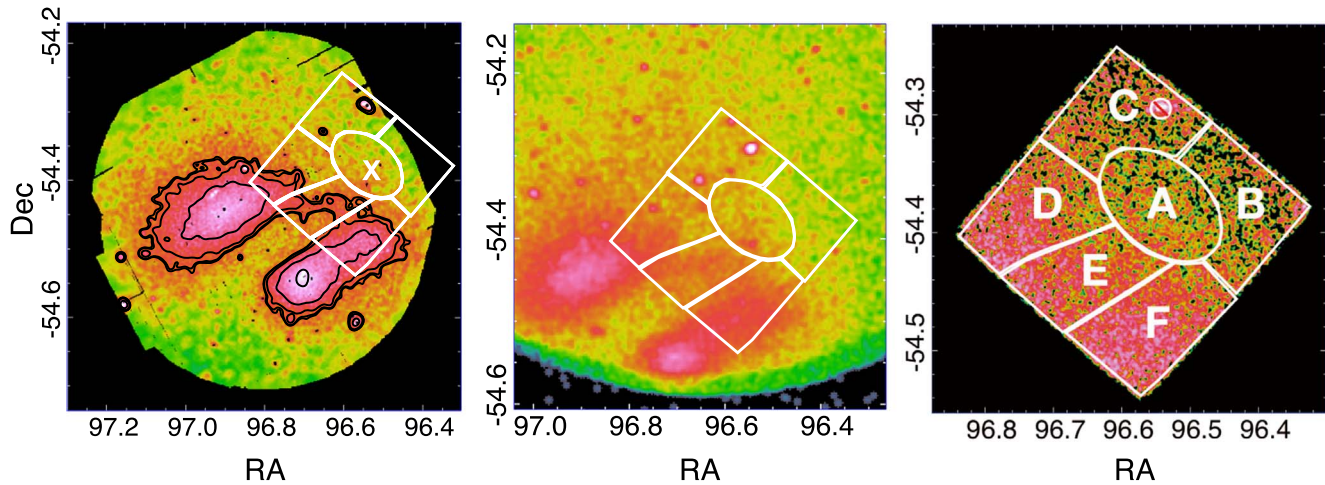


**Figure 7.** Regions of interest superimposed on photon images of A3395 from 0.4–2.5 keV XMM-Newton (left panel), binned event file eROSITA (middle panel), and 3.0–20.0 keV NuSTAR (right panel). The X label on the XMM-Newton image indicates the location of the hot spot found in the literature (Lakhchaura et al. 2011).

lie near the FOV of the NuSTAR pointing. Our FOV covers distances of  $3'$ – $20'$  from either of the subcluster centers, where the scattered light contamination is known to be significant (Madsen et al. 2017).

We did not study the effect of the back reflection contamination, since this component appears at very high fluxes and becomes effective at  $\sim 15'$ , whereas the largest distance covered by our NuSTAR FOV from either of the subcluster centers is  $\sim 20'$ . Also, the relative geometric area, i.e., fraction of back reflection to on-axis geometric area, is below 1% between  $15'$  and  $20'$  (Madsen et al. 2017).

To model the scattered light, we used the ray-tracing code for X-ray telescopes, MT\_RAYOR (version 4.6.9) (Westergaard 2011) written in Yorick interpreted language (Munro & Dubois 1995), to simulate the properly focused photons (good photons) and photons that undergo single reflection (scattered light). MT\_RAYOR takes a count rate image in the 0.5–2.5 keV energy band and a temperature map constructed from other X-ray missions—XMM-Newton in this case—guided by literature (Lakhchaura et al. 2011), as an input for the distribution of photons in the cluster, divides the cluster into predefined pixels, and predicts the expected double and single bounce photons from a NuSTAR observation, mainly treating the extended ICM emission as a collection of point sources that have different spectral properties as well as photon distributions.

These MT\_RAYOR simulations provide a spatial distribution of good photons as well as the scattered light. We then extracted spectra from the six regions from both the good photons and scattered light simulation results (Figure 8). Good photons describing the cluster emission were then fit by a single *apec* model, whereas we applied different models to fit the scattered light to find the best model that describes this contamination. We used *apec*, *powerlaw*, and *bknpower* models and find that *powerlaw* is the best model describing the scattered light for all regions. The model *powerlaw* has two parameters, photon index ( $\Gamma$ ) and model normalization ( $\kappa$ ). The resulting photon indices are presented in Table 3. The spectral fits of the simulated regions are shown in Figure 13 in Appendix B.

We also created maps of hardness ratio with a selection of different energy bands to investigate the energy dependence of

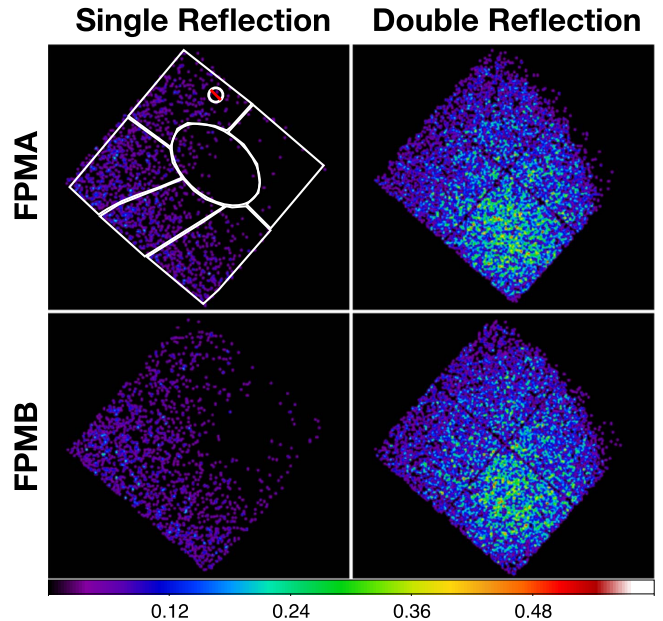


**Figure 8.** Ray-trace simulation results obtained from MT\_RAYOR indicating single-reflection photons (scattered light, left panel), and photons that are properly focused (right panel) on the focal plane modules A (FPMA, top panel) and B (FPMB, bottom panel). Regions of interest are overlaid on the FPMA scattered light photon distribution.

the spatial distribution of the ray-traced scattered light, yet no apparent gradient was observed.

Once we calculated the 3–15 keV flux from both the good photons and scattered light for all six regions of interest, we deduced the ratio of the scattered photons to the total photons as presented in Table 3. The flux ratios as well as simulated images showed that the main region of interest, i.e., Region A, showed very little contamination from the scattered light. Since the number of ray-trace-simulated photons may differ from the real data, direct addition of the ray-traced scattered light spectra to the background spectrum may result in overestimation or underestimation of scattered light. Therefore, we calculated the fluxes from all six regions of the observational data, then with the 3–15 keV flux ratios provided from the aforementioned analysis, we used the *fakeit* function of XSPEC to simulate the scattered light with the previously obtained fitted parameter



**Table 3**  
Photon Index ( $\Gamma$ ) Values from a `powerlaw` Fit of Ray-traced NuSTAR Scattered Light for the Regions of Interest in the Energy Band 3–15 keV

	Region A	Region B	Region C	Region D	Region E	Region F
FPMA	2.44 (1.98%)	N/A (<1%)	2.64 (11.0%)	2.28 (23.3%)	2.31 (12.4%)	2.45 (10.4%)
FPMB	3.50 (2.21%)	2.01 (4.19%)	2.40 (10.8%)	2.53 (24.0%)	2.67 (14.8%)	2.14 (12.9%)

**Note.** The scattered light flux percentages with respect to total photons are given in parenthesis.

$\Gamma$ , and reset the model norms to match the flux-estimated ray-trace flux ratios. Our recipe is summarized in the flow chart in Figure 9.

### 3.4. The NuSTAR, XMM-Newton, Suzaku, and Joint NuSTAR and XMM-Newton Analysis of Regions of Interest

We fitted the `apec` model to the XMM-Newton spectrum extracted from the six ROIs. In this analysis, the abundance was a free parameter, and we present best-fit results where  $n_{\text{H}}$  is fixed to the literature value of  $n_{\text{H}} = 6.30 \times 10^{20} \text{ cm}^{-2}$  (Lakhchaura et al. 2011) in Table 4.

The faked spectra of each region were added to the corresponding background model spectra using `addspec` script by HEASoft `ftools`. After combining the scattered light and `nuskybgd` background, we fit the NuSTAR observational data with an `apec` model for the six regions, and the results are shown in Table 4.

For comparison and to see the effect of scattered light on model parameters, we also repeated the analysis without including our scattered light analysis. The results for this secondary analysis are shown in Table 4.

We also repeated the spectral analysis for the same six ROIs using Suzaku data. The result of the fits are presented in Table 4.

As the next step, we fitted NuSTAR and XMM-Newton spectra jointly for all six ROIs, where the abundance values were fixed to the values obtained from XMM-Newton spectral fits. The results are shown in Table 4.

We also jointly fitted the NuSTAR and XMM-Newton spectra from the regions of interest using an additional `apec` or `powerlaw` component to the original `apec` model. From these regions, the emission coming from Regions A and E is found to be better described with an additional spectral model.

Region A hints at a two-temperature structure, the high-temperature component being  $kT = 16.2 \text{ keV}$ , for which only a lower limit of  $8.5 \text{ keV}$  is obtained. The lower temperature is found to be  $kT = 2.90^{+0.47}_{-0.29} \text{ keV}$ . This `apec + appec` model improved the statistics by  $\Delta C/\Delta\nu = 12.47/2$ . Applying `apec + powerlaw` model also improved the statistics ( $\Delta C/\Delta\nu = 12.36/2$ ), giving a photon index of  $\Gamma = 1.70^{+0.23}_{-0.62}$ .

An additional `apec` component improved the statistics of the Region E spectrum with respect to the single `apec` model by  $\Delta C/\Delta\nu = 19.42/2$ . This two-temperature model resulted in a high-temperature component of  $kT = 15.91^{+15.92}_{-4.70} \text{ keV}$  and a low temperature component of  $kT = 3.78^{+0.37}_{-0.32} \text{ keV}$ . Instead, when the `apec + powerlaw` model was used, the statistics were improved by  $\Delta C/\Delta\nu = 24.41/2$ . This combined model resulted in a power-law emission with a photon index of  $\Gamma = 1.80^{+0.12}_{-0.17}$ , and the thermal component was  $kT = 4.28^{+0.57}_{-0.27} \text{ keV}$ .

Since we did not find a constrained, strong high-temperature component in Region A, we restricted our spectral analysis to a smaller region with  $r = 1/5$  centered at the X shown in Figure 7.

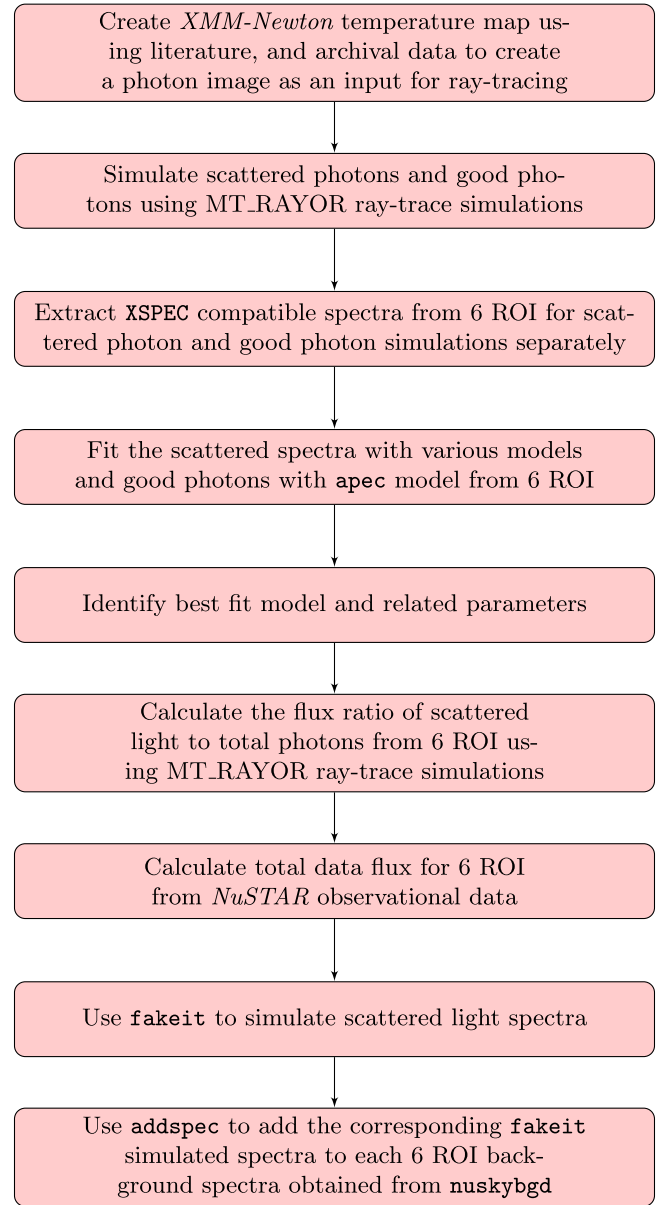


**Figure 9.** Scattered light recipe.

We fitted an `apec` model to the joint NuSTAR and XMM-Newton spectra and the XMM-Newton spectrum alone. For these analyses, we used both fixed and free abundance and  $n_{\text{H}}$  parameters, having eight different spectral fits. The abundance was fixed to  $Z = 0.23 Z_{\odot}$  as obtained from the XMM-Newton spectral fit for Region A. We present the results of this analysis in Appendix C.

We also created deprojected thermodynamical maps using the XSPEC model `apcc`, which is defined as

**Table 4**  
Spectral Parameters of XMM-Newton (0.5–9.0 keV), NuSTAR (3.0–15.0 keV), and Suzaku (0.7–7.0 keV) Analysis for the Regions of Interest

Regions	Spectral Parameters	XMM-Newton <sup>a</sup>	NuSTAR with SL Treatment	NuSTAR without SL Treatment	Suzaku <sup>b</sup>	Joint NuSTAR <sup>b</sup> and XMM-Newton
A	$kT$ (keV)	$4.46^{+0.78}_{-0.49}$	$3.74^{+0.40}_{-0.34}$	$3.74^{+0.40}_{-0.33}$	$5.14^{+0.52}_{-0.44}$	$3.78^{+0.36}_{-0.15}$
	$Z$ ( $Z_{\odot}$ )	$0.23^{+0.23}_{-0.16}$	0.23 (fixed)	0.23 (fixed)	$0.14 \pm 0.13$	0.23 (fixed)
	$norm$ ( $\text{cm}^{-5}$ )	$2.99^{+0.17}_{-0.22} \times 10^{-5}$	$1.49^{+0.20}_{-0.18} \times 10^{-3}$	$1.52^{+0.20}_{-0.18} \times 10^{-3}$	$3.00^{+0.16}_{-0.15} \times 10^{-3}$	$2.97^{+0.09}_{-0.14} \times 10^{-5}$
	( $C$ or $\chi^2$ )/ $\nu$	375.85/351	649.30/587	651.16/587	387/413	1695.97/1974
B	$kT$ (keV)	$5.17^{+3.51}_{-1.92}$	$3.55^{+0.66}_{-0.47}$	$3.70^{+0.61}_{-0.54}$	$4.72^{+0.69}_{-0.59}$	$3.55^{+0.60}_{-0.45}$
	$Z$ ( $Z_{\odot}$ )	$0.18^{+0.96}_{-0.18}$	0.18 (fixed)	0.18 (fixed)	$0.09^{+0.20}_{-0.09}$	0.18 (fixed)
	$norm$ ( $\text{cm}^{-5}$ )	$2.23^{+0.47}_{-0.52} \times 10^{-5}$	$1.51^{+0.33}_{-0.29} \times 10^{-3}$	$1.43^{+0.34}_{-0.24} \times 10^{-3}$	$1.91^{+0.17}_{-0.16} \times 10^{-3}$	$2.15^{+0.28}_{-0.27} \times 10^{-5}$
	( $C$ or $\chi^2$ )/ $\nu$	128.30/108	634.71/595	636.99/595	211/252	1049.24/1133
C	$kT$ (keV)	$4.41^{+1.02}_{-0.84}$	$3.00^{+0.59}_{-0.41}$	$3.17^{+0.57}_{-0.41}$	$4.65^{+0.43}_{-0.41}$	$3.34^{+0.44}_{-0.38}$
	$Z$ ( $Z_{\odot}$ )	$0.44^{+0.44}_{-0.27}$	0.44 (fixed)	0.44 (fixed)	$0.17 \pm 0.13$	0.44 (fixed)
	$norm$ ( $\text{cm}^{-5}$ )	$2.43^{+0.30}_{-0.32} \times 10^{-5}$	$2.06^{+0.50}_{-0.43} \times 10^{-3}$	$2.13^{+0.46}_{-0.40} \times 10^{-3}$	$2.84^{+0.16}_{-0.15} \times 10^{-3}$	$2.37^{+0.15}_{-0.16} \times 10^{-5}$
	( $C$ or $\chi^2$ )/ $\nu$	299.07/253	618.81/584	629.15/584	388/420	1442.07/1652
D	$kT$ (keV)	$4.95^{+0.39}_{-0.38}$	$4.01^{+0.44}_{-0.37}$	$4.41^{+0.39}_{-0.34}$	$5.30^{+0.42}_{-0.33}$	$4.33^{+0.28}_{-0.26}$
	$Z$ ( $Z_{\odot}$ )	$0.25^{+0.10}_{-0.11}$	0.25 (fixed)	0.25 (fixed)	$0.21 \pm 0.11$	0.25 (fixed)
	$norm$ ( $\text{cm}^{-5}$ )	$4.89^{+0.15}_{-0.19} \times 10^{-5}$	$2.23^{+0.29}_{-0.26} \times 10^{-3}$	$2.56^{+0.25}_{-0.23} \times 10^{-3}$	$4.60^{+0.19}_{-0.18} \times 10^{-3}$	$5.03^{+0.14}_{-0.13} \times 10^{-5}$
	( $C$ or $\chi^2$ )/ $\nu$	685.84/611	588.59/585	615.74/585	572/559	2224.15/2548
E	$kT$ (keV)	$5.16^{+0.41}_{-0.37}$	$5.31^{+0.53}_{-0.44}$	$5.31^{+0.49}_{-0.42}$	$5.57^{+0.52}_{-0.40}$	$5.00^{+0.30}_{-0.28}$
	$Z$ ( $Z_{\odot}$ )	$0.37^{+0.13}_{-0.10}$	0.37 (fixed)	0.37 (fixed)	$0.18 \pm 0.12$	0.37 (fixed)
	$norm$ ( $\text{cm}^{-5}$ )	$5.32^{+0.22}_{-0.23} \times 10^{-5}$	$1.58^{+0.14}_{-0.13} \times 10^{-3}$	$1.60^{+0.13}_{-0.12} \times 10^{-3}$	$(5.14 \pm 0.22) \times 10^{-3}$	$(5.41 \pm 0.12) \times 10^{-5}$
	( $C$ or $\chi^2$ )/ $\nu$	667.32/610	659.01/580	670.20/580	498/47	2262.75/2502
F	$kT$ (keV)	$4.81^{+0.28}_{-0.24}$	$5.27^{+0.39}_{-0.34}$	$5.49 \pm 0.35$	$5.65^{+0.54}_{-0.44}$	$4.82^{+0.22}_{-0.20}$
	$Z$ ( $Z_{\odot}$ )	$0.14^{+0.06}_{-0.07}$	0.14 (fixed)	0.14 (fixed)	$0.12 \pm 0.12$	0.14 (fixed)
	$norm$ ( $\text{cm}^{-5}$ )	$8.60^{+0.18}_{-0.21} \times 10^{-5}$	$2.62^{+0.19}_{-0.18} \times 10^{-3}$	$2.79^{+0.19}_{-0.16} \times 10^{-3}$	$7.00^{+0.30}_{-0.29} \times 10^{-3}$	$8.73^{+0.11}_{-0.14} \times 10^{-5}$
	( $C$ or $\chi^2$ )/ $\nu$	919.68 / 890	621.19/594	630.87/594	433/450	2631.39/2926

**Notes.**  $ap\text{ec}$  normalization ( $norm$ ) is given by  $\frac{10^{-14}}{4\pi[D_A(1+z)]^2} \int n_e n_H dV$ .

<sup>a</sup>  $\chi^2$  is used.

<sup>b</sup> Scattered light (SL) treatment is included.

$[10^{-14}/4\pi[D_A(1+z)]^2] \int n_e n_H dV$ , to obtain electron density  $n_e$ , with the assumption of a fully ionized plasma,  $n_e \simeq 1.2 n_H$ . For the volume, we used the area of the ROI obtained using SAOImageDS9<sup>16</sup> multiplied by the depth, and for the depth we assumed 1 Mpc for the line of sight (LOS), therefore the density values are scaled by  $(\text{LOS}/1 \text{ Mpc})^{-1/2}$  similar to the approach adopted by Akamatsu et al. (2017). For entropy and electron pressure, we used the commonly adopted definitions,  $S = kT \times n_e^{-2/3}$  (scaled by  $(\text{LOS}/1 \text{ Mpc})^{1/3}$ ) and  $P_e = n_e \times kT (\text{LOS}/1 \text{ Mpc})^{-1/2}$ , respectively (Gitti et al. 2010). Gas pressure then becomes  $P = n \times kT$ , where we assume  $n = 2n_e$ . The resulting maps are shown in Figure 10, and the corresponding errors are given in Table 5.

We made two more assumptions for LOS for our thermodynamical values to be easily compared with future work. First, we adopted  $r_{180} = 34.6$  (Markevitch et al. 1998) and  $r_{180} = r_{\text{vir}}$ , and estimated the distance of the center of each region from the midpoint of subcluster centers of A3395. The distances ( $x$ ) we find for regions A, B, C, D, E, and F are 637 kpc ( $\sim 0.32 r_{\text{vir}}$ ), 876 kpc ( $\sim 0.44 r_{\text{vir}}$ ), 776 kpc ( $\sim 0.39 r_{\text{vir}}$ ), 438 kpc ( $\sim 0.22 r_{\text{vir}}$ ), 338 kpc ( $\sim 0.17 r_{\text{vir}}$ ), and 458 kpc ( $\sim 0.23 r_{\text{vir}}$ ), respectively.

These estimated distances are used for a secondary estimation of LOS. Along the center of the cluster where

$x = 0$  and  $\theta = 0$ , the depth is  $2r_{500} \sim 2$  Mpc, and then it scales with varying  $[x, \theta]$ . The given distances ( $x$ ) for these regions can be used as  $\sin(\theta)$ , where LOS is  $2\cos(\theta)$  assuming a perfect sphere with  $r = r_{\text{vir}}$ . With these assumptions, LOS for regions A, B, C, D, E, and F becomes  $\sim 1.33$  Mpc,  $\sim 0.62$  Mpc,  $\sim 1.02$  Mpc,  $\sim 1.64$  Mpc,  $\sim 1.73$  Mpc, and  $\sim 1.62$  Mpc, respectively.

A third estimation for LOS is achieved by using  $r_{\text{vir}}$  instead of  $r_{500}$ . This time, along the center of the cluster where  $x = 0$  and  $\theta = 0$ , the depth is  $2r_{\text{vir}} \sim 4$  Mpc, and then it again scales with varying  $[x, \theta]$ . We now assume  $r = r_{\text{vir}}$ . With these assumptions, LOS for regions A, B, C, D, E, and F becomes  $\sim 3.76$  Mpc,  $\sim 3.56$  Mpc,  $\sim 3.68$  Mpc,  $\sim 3.90$  Mpc,  $\sim 3.92$  Mpc, and  $\sim 3.89$  Mpc, respectively.

Using these physical distances along with the scaling factors used for density  $((\text{LOS}/1 \text{ Mpc})^{-1/2})$ , entropy  $((\text{LOS}/1 \text{ Mpc})^{1/3})$ , and pressure  $((\text{LOS}/1 \text{ Mpc})^{-1/2})$ , results presented in Table 5 can easily be used with future work depending on the choice of radius for the cluster emission.

We also calculated the luminosity of the cluster from the XMM-Newton spectra within  $r = 796'' = 0.83r_{500}$ , adopting  $r_{500} = 930$  kpc =  $954''$  (Alvarez et al. 2018). This selected region covers the whole FOV of the XMM-Newton observation. We find the X-ray bolometric (0.01–100 keV) luminosity to be  $L_X = 2.342^{+0.015}_{-0.011} 10^{44} \text{ erg s}^{-1}$ , and within 0.5–2.0 keV we

<sup>16</sup> <https://sites.google.com/cfa.harvard.edu/saoimageds9>

**Table 5**

Deprojected Thermodynamical Parameters from NuSTAR (3.0–15.0 keV) Spectral Fits for the Regions of Interest where the Scattered Light Emission Is Included

	Region A	Region B	Region C	Region D	Region E	Region F
Area (arcmin <sup>2</sup> )	25.4	28.5	20.8	24.9	20.3	23.9
$n_e$ ( $10^{-4}$ cm <sup>-3</sup> )	$6.74^{+0.42}_{-0.41}$	$6.40^{+0.61}_{-0.70}$	$8.75^{+1.06}_{-0.91}$	$8.32^{+0.54}_{-0.49}$	$7.77^{+0.34}_{-0.32}$	$9.21^{+0.33}_{-0.32}$
$S$ (keV cm <sup>2</sup> )	$486^{+56}_{-48}$	$478^{+95}_{-70}$	$328^{+70}_{-50}$	$453^{+53}_{-45}$	$628^{+65}_{-55}$	$557^{+43}_{-38}$
$P$ ( $10^{-12}$ dyn cm <sup>-2</sup> )	$4.04^{+0.51}_{-0.44}$	$3.64^{+0.78}_{-0.59}$	$4.21^{+0.97}_{-0.72}$	$5.35^{+0.68}_{-0.58}$	$6.61^{+0.72}_{-0.61}$	$7.77^{+0.64}_{-0.57}$

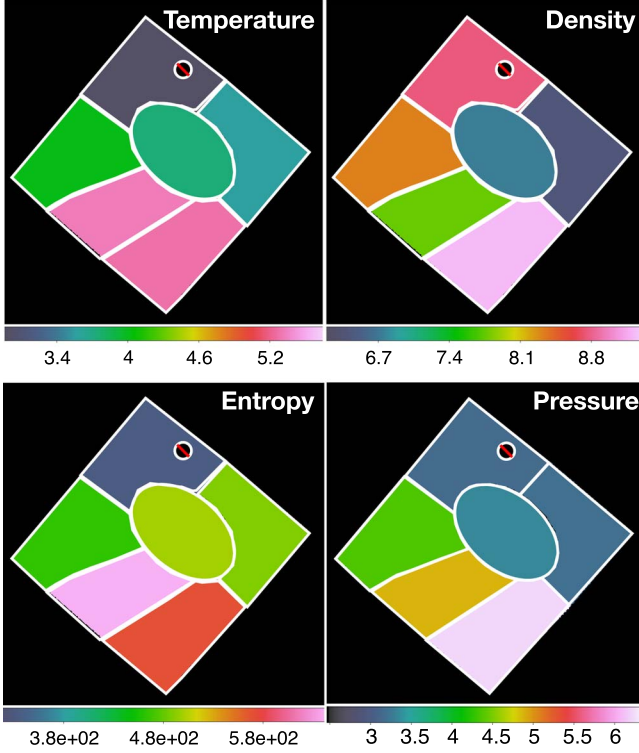


**Figure 10.** Maps of NuSTAR temperature (upper left), deprojected density (upper right), deprojected entropy (lower left), and deprojected pressure (lower right) for regions of interest. Temperature is given in units of keV, density is given in units of  $10^{-4}$  cm<sup>-3</sup> scaled by  $(\text{LOS}/1 \text{ Mpc})^{-1/2}$ , entropy is in units of keV cm<sup>2</sup> scaled by  $(\text{LOS}/1 \text{ Mpc})^{1/3}$ , and pressure is presented in units of  $10^{-12}$  dyn cm<sup>-2</sup> scaled by  $(\text{LOS}/1 \text{ Mpc})^{-1/2}$ .

find  $L_X = 1.204^{+0.041}_{-0.071} 10^{44}$  erg s<sup>-1</sup> using XSPEC convolution model `clumin`. Within this region, we find  $kT = 4.37 \pm 0.04$  keV for the 0.5–7.0 keV band using a single-temperature model. In Figure 11, we added the core X-ray properties of A3395 (black dot) to the bolometric luminosity versus X-ray temperature scaling relation presented in Gaspari et al. (2014). We note that since the error bars are small, they are contained within the black dot, which is enlarged to facilitate its differentiation from the rest of the sample.

### 3.5. The Point Source in Region C

We also analyzed the spectral properties of the point source residing inside Region C previously cataloged as 2MASX J06261214-5417071 at  $z = 0.05050$  (SIMBAD, Donnelly et al. 2001; Paturel et al. 2003; Jones et al. 2009; Marziani et al. 2017). We extracted a circular region of  $r = 1''.2$  centered on the point source. We find that the best-fit model that describes the emission from the source in the 3–20 keV band is an `appec` + `powerlaw` model with a photon index of  $\Gamma = 1.48^{+0.56}_{-0.83}$  and  $C/\nu = 412.10/457$ . The plasma temperature was found to be

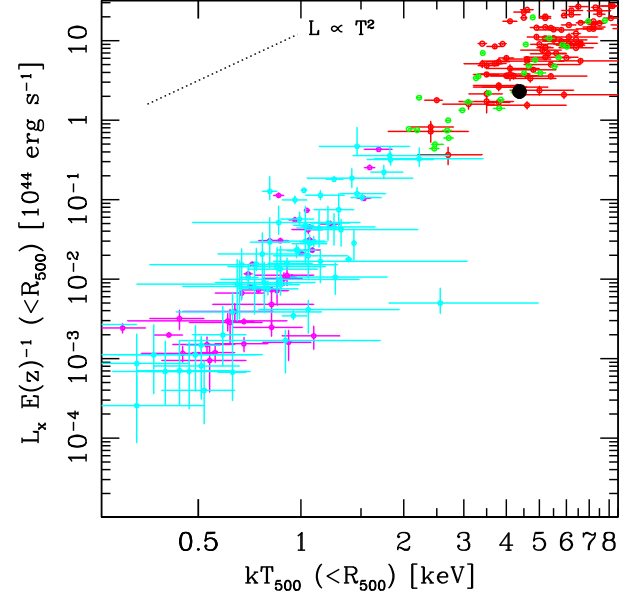


**Figure 11.** X-ray bolometric luminosity vs. X-ray temperature (adapted from Gaspari et al. 2014; see this paper for the samples of groups/clusters included with different colors). A3395 is superimposed with a black dot.  $E(z)$  is the cosmological evolution factor, of near unitary value. It clearly touches the lower envelope of the scaling relation, which is the typical location of non-cool-core systems.

$kT = 1.81^{+0.95}_{-0.59}$  keV with  $Z = 0.43^{+2.47}_{-0.31} Z_\odot$ . The luminosity of the powerlaw component is found to be  $L_X = 1.434^{+0.153}_{-0.166} 10^{42}$  erg s<sup>-1</sup> within 3.0–20.0 keV and  $L_X = 5.962^{+0.706}_{-0.676} 10^{40}$  erg s<sup>-1</sup> within 0.5–2.0 keV. For the `appec` component, we found the 3.0–20.0 keV luminosity to be  $L_X = 7.330^{+1.008}_{-0.977} 10^{41}$  erg s<sup>-1</sup> and the 0.5–2.0 keV luminosity is  $L_X = 3.333^{+0.458}_{-0.444} 10^{41}$  erg s<sup>-1</sup>.

This two-component model improved the statistics with respect to a single-temperature model by  $\Delta C/\Delta \nu = 14.15/2$ . The single-temperature model resulted in  $kT = 6.44^{+0.86}_{-0.74}$  keV plasma with an unconstrained abundance value. When we freed the redshift, we found  $z = 0.061^{+0.025}_{-0.028}$ , which agrees with both the cluster and source (2MASX J06261214-5417071, Jones et al. 2009) redshifts within  $1\sigma$ .

We extracted a spectrum using the same region from XMM-Newton data. We grouped the XMM-Newton spectrum by 3 as well and applied `cstat` for direct comparison with NuSTAR results. A single-temperature model indicates  $kT = 4.64^{+0.60}_{-0.37}$  keV plasma with  $Z = 0.58^{+0.25}_{-0.30} Z_\odot$ . An addition of a powerlaw component did not improve the fit and the photon index was not constrained. However, a single powerlaw model fit without an `appec` component gives a photon index of  $\Gamma = 1.90^{+0.05}_{-0.09}$ . Since these two emission models can be degenerate within XMM-Newton operating energy band given the similar statistics, we extracted a spectrum in the vicinity of



the point source with the same area, and characterized the ICM within that region. A single-temperature model in this region showed a plasma with  $kT = 3.04_{-0.76}^{+1.83}$  keV and  $Z = 0.36_{-0.25}^{+0.87} Z_{\odot}$ . The parameters obtained from the `apec` fit of the region in the vicinity of the point source were then inserted and fixed during the fitting procedure of the point source, where a combined `apec + powerlaw` model was implemented. We then found a photon index of  $\Gamma = 1.86_{-0.11}^{+0.10}$  for the `powerlaw` component. Within 0.5–2.0 keV, we estimate a luminosity of  $L_X = 3.555_{-0.279}^{+0.308} 10^{41}$  erg s<sup>-1</sup> again for the `powerlaw` component.

#### 4. Discussion

We studied NuSTAR, XMM-Newton, and Suzaku data of the merging cluster A3395. In this section, we discuss our results in relation to the literature.

##### 4.1. On the Global Properties

For the NuSTAR data of A3395, we first considered the global spectrum of the part of the cluster within the FOV, which was fit to a single-temperature thermal plasma model (`apec`). We found an average temperature of  $kT = 5.59 \pm 0.11$  keV. Although this is the global result from the NuSTAR FOV, the pointing only covers the northwestern part of the cluster, and therefore this is not the global temperature of the cluster itself. However, the lack of a good fit suggests a single-temperature model insufficiently describes the data. As this is a merging cluster, we cannot assume isothermality across the FOV, and we expect the FOV to be contaminated by scattered light due to the presence of the subcluster centers in the vicinity of the pointing. We therefore fit this spectrum with two more models, with either an additional `apec` or `powerlaw` component.

We find that the `apec+powerlaw` model better describes the global spectrum with  $kT = 2.06_{-0.22}^{+0.31}$  keV and  $\Gamma = 1.82_{-0.29}^{+0.18}$ . However, this  $\simeq 2$  keV temperature is much smaller than expected based on the results of Markevitch et al. (1998), Donnelly et al. (2001), and Lakhchaura et al. (2011). In addition, the single-temperature model result of  $\simeq 5.6$  keV is then higher than the global temperatures found for the cluster by Markevitch et al. (1998), Donnelly et al. (2001), Lakhchaura et al. (2011), and Alvarez et al. (2018). The global temperatures they report account for the hot plasma at the cluster center and the NuSTAR FOV does not cover the central region of A3395. The cluster temperatures are expected to drop with increasing radius, assuming there are no shocks. The  $\simeq 5.6$  keV result we find for NuSTAR FOV should be even lower than their reported values and not higher. Although Lakhchaura et al. (2011) points to high-temperature regions enclosed in our NuSTAR FOV, which gave a motivation to study these regions in detail with NuSTAR, we recall that they also state a 60% error on these values.

Further investigating the impact of scattered light, we found that its contribution could also be modeled with a `powerlaw` model. This fact, combined with the presence of gas at different temperatures, suggests that the `apec+powerlaw` model is sufficiently flexible to capture these more extensive components and that the `powerlaw` component should not be interpreted to have physical meaning. Therefore, taking advantage of NuSTAR’s imaging capability, we continued with a grid analysis as described in Section 3.2. This analysis

and the XMM-Newton photon image (upper panel of Figure 7) showed that there are six regions in the NuSTAR FOV with similar thermodynamical properties and substructures.

We also studied the XMM-Newton FOV that covers the central  $\sim 0.83r_{500}$  of the cluster to obtain the global temperature and luminosity of the cluster. Our temperature result is  $kT = 4.37 \pm 0.04$  keV, which is in agreement with the literature (Markevitch et al. 1998; Donnelly et al. 2001) within  $1\sigma$  errors. We found a luminosity of  $L_X = 1.204_{-0.071}^{+0.041} 10^{44}$  erg s<sup>-1</sup> within 0.5–2.0 keV, which is in agreement with the luminosity estimation of De Grandi et al. (1999) within  $1\sigma$ . We found the X-ray bolometric (0.01–100 keV) luminosity to be  $L_X = 2.342_{-0.011}^{+0.015} 10^{44}$  erg s<sup>-1</sup>, as plotted in the  $L_X$ – $T_X$  scaling relation in Figure 11. Cool-core systems tend to reside in the upper envelope of the scaling relation due to a higher  $L_X$  per given  $T_X$  (or  $M_{\text{total}}$  since  $T_X$  is a tight proxy for cluster mass), whereas merging clusters whose cool cores have been disrupted reside in the lower envelope (Gaspari et al. 2014). A3395 lies at the lower boundary, in agreement with the typical behavior of the population of non-cool-core clusters, which do not have the inner cool region of the ICM. This suggests that A3395 might have evacuated significant gas mass (moving toward the bottom), heated the gas (moving toward the right), or this cluster has assembled in a poor gas environment. Having a hot ( $\sim 6$  keV) intracluster filament in between its subclusters (Region E in our analysis, Region 2 in Markevitch et al. 1998, Region 3 in Donnelly et al. 2001, Region F in Lakhchaura et al. 2011), and lacking a cool core, A3395 appears to be still in an early stage of merger, since it lacks a major overheating.

##### 4.2. On the Treatment of Scattered Light

Using ray-trace simulations with `MT_RAYOR`, we assessed the scattered light contamination in our observation. We find that the scattered light is best modeled with a `powerlaw`, and we provide a quantitative description of this contamination. This is an empirical model and due to the nonuniformity of the scattered light contamination, its complete behavior needs to be assessed with further studies of the off-axis angle and source energy dependence, as well as the position on the detector. This is a multidimensional problem, and our method is the only known approach to study NuSTAR data that has scattered light contamination, to the best of our knowledge. The method is described in detail in Section 3.3, and the method is summarized in the flow chart shown in Figure 9.

We find that in Regions A and B, where A3395 connects with an intercluster filament, the scattered light contamination is below 5% of the total flux. Regions C, D, and F suffer from scattered light at the  $\sim 15\%$  level, and this contamination rises to  $\sim 25\%$  for Region E. This is expected since Region E is near both of the bright subcluster centers, namely the NE and SW regions denoted in the upper panel of Figure 7.

A quick comparison of C-stat values of NuSTAR spectral fits with and without SL treatment in Table 4 shows that the fits improved for all ROIs when the scattered light component is included, with  $\Delta C$  ranging from  $\sim 2$  to  $\sim 27$ . Thus, the inclusion of our scattered light as an additional background component results in a better assessment of the source emission. However, we note that for all ROIs, the NuSTAR temperature results from the spectra with and without scattered light treatment agree within  $1\sigma$ . Our temperature results from the NuSTAR data are in agreement to those from the XMM-Newton and joint NuSTAR and XMM-Newton analyses for a

region with  $\sim 25\%$  scattered light contamination within  $1\sigma$ . Our results show that, for regions of interest where scattered light contamination is above 10% (Regions C, D, E, and F), the temperature values are in agreement within  $1.6\sigma$  for NuSTAR, XMM-Newton, Suzaku, and joint XMM-Newton and NuSTAR spectral fits, which validates our approach to tackling the NuSTAR scattered light contamination for this observation.

We claim that, although the effect of scattered light contamination depends on the flux and emission features of structures, at a level of up to  $\sim 25\%$ , we seem to be safe within  $1\sigma$  errors of the face value of temperature. However, we also note that further investigation is needed to fully understand the effect of scattered light at various plasma temperatures. Our technique can be used for future NuSTAR observation proposals to estimate the possible scattered light contamination.

#### 4.3. On the Regions of Interest

NuSTAR temperature results from all regions of interest seem to be lower than what is found with Suzaku (Table 4). This trend is also seen in regions A, B, C, and D for NuSTAR versus XMM-Newton. Cross-calibration studies similar to XMM-Newton and Chandra by Schellenberger et al. (2015) are required for NuSTAR, XMM-Newton, and Suzaku to understand this behavior.

In our detailed analysis of the possible connection region of the cluster with the intercluster filament, Region A, we cannot confirm the existence of a strong high-temperature component in any of our NuSTAR, XMM-Newton, Suzaku, and joint NuSTAR and XMM-Newton fits, as previously reported in the temperature map of Lakhchaura et al. (2011). We consistently find temperature values around 4–5 keV in all data sets considered. This region is also present in a temperature map based on ASCA observations (Markevitch et al. 1998), and our temperature results from NuSTAR, XMM-Newton, Suzaku, and joint NuSTAR and XMM-Newton fits all agree with their results within  $1\sigma$ . However, Lakhchaura et al. (2011) do note 60% errors on their map for regions lying at the edge of the FOV of the XMM-Newton pointing due to the low S/N.

Although we find a high-temperature component ( $\sim 16$  keV) for Region A with NuSTAR analysis, where a two-temperature plasma model was applied to the spectrum, only a lower bound ( $\sim 8$  keV) for this higher-temperature component is found; the ICM is mainly dominated by the cooler component ( $\sim 4$  keV).

To better isolate a possible hot spot lying in Region A, we extracted spectra in a smaller region ( $r = 1.5'$ ) from both NuSTAR and XMM-Newton, centered on the hottest region in the XMM-Newton temperature map reported by Lakhchaura et al. (2011). During these fitting procedures, we investigated the effect that column density and abundance may have on the temperature measurements, due to the possible bias against XMM-Newton temperatures caused by the uncertainties in effective area at soft energy (Schellenberger et al. 2015). While keeping  $n_{\text{H}}$  frozen, we first kept the  $Z$  parameter fixed to the value found from the XMM-Newton analysis of Region A. Then we fit the spectra again by allowing  $Z$  to be free. We repeated the same process by freeing  $n_{\text{H}}$ .

The highest temperature we find is  $kT = 5.13^{+1.80}_{-1.48}$  keV with our XMM-Newton analysis (Table 6). We found lower temperatures with a joint XMM-Newton and NuSTAR analysis than with the XMM-Newton analysis alone (Table 7). In addition, all temperature values from these procedures agree within  $1\sigma$ . Since background dominates at the edge of the

XMM-Newton FOV, we hypothesize that the discrepancy between our results and the literature at the hot spot location may be due to how the background was treated; for example, the background model of Lakhchaura et al. (2011) might underestimate the true background at those locations.

Region B is also located near the connection region of A3395 and the intercluster filament. This region was also partially covered by the analysis of Markevitch et al. (1998), whose temperature results agree with ours at the  $1\sigma$  level. Regions C and D are at least partly included in the NW region studied by Lakhchaura et al. (2011), where our XMM-Newton temperature result agrees with their findings within  $1\sigma$ .

The bridge emission between the two subclusters of A3395 enclosed by our Region E shows high temperature, entropy, and pressure with respect to the surrounding ICM. Moreover, this region was well fit by a two-temperature plasma model. This bridge is thought to be ram pressure-stripped from the northern subcluster in the A3395 merging system. Lakhchaura et al. (2011) finds a higher temperature for this *intracluster* filament than we do, yet our temperature value is within  $1.5\sigma$  of theirs.

In addition, we searched for a nonthermal X-ray counterpart of the faint extended radio source to the west of A3395, lying in our Region F (Reiprich et al. 2021). They argue they this source, denoted as S2/S3 in their work, may be a radio relic or may be due to reaccelerated relativistic plasma. We find no significant nonthermal emission in this region, possibly because the hot ICM dominates the emission.

The electron entropy is closely related to the thermodynamical history of the clusters (Voit et al. 2005). In particular, the entropy of the ICM decreases in the process of radiative cooling and increases when heating energy is introduced into the ICM, e.g., via merging and feedback processes (Gaspari 2015). And at the interface regions of cluster outskirts and WHIM filaments is the zone where entropy flattening is observed (Alvarez et al. 2018). To assess the merger history of the cluster and possible interaction of the filament and the cluster, we estimated the entropy for our ROIs. Since it is difficult to create radial profiles of a sample of non-cool-core systems due to asymmetrical morphology as well as non-thermal processes caused by mergers, we compared the entropy values with the 13 nearby cooling-flow cluster entropy profiles studied by Piffaretti et al. (2005, Figure 5) in the following paragraph.

In order to make this comparison, we used the distance estimations of regions explained in Section 3.4. For Region A at  $\sim 0.32r_{\text{vir}}$ , we find the entropy to lie below the fitting curve yet within the scatter of the sample, and in addition, within  $1\sigma$  of galaxy cluster 2A 0335+096. Region B, at  $\sim 0.44r_{\text{vir}}$ , again is at the lower boundary of the scatter, in agreement with the entropy of Sérsic 159-3 at the same distance from the core. Region C (at  $\sim 0.39r_{\text{vir}}$ ) has a lower entropy than the whole sample range. The entropy of Region D at  $\sim 0.22r_{\text{vir}}$  is within the sample entropy values, still lying below the mean. The entropy of Region E ( $\sim 0.17r_{\text{vir}}$ ) lies above the fitted curve. Finally, the entropy value of Region F ( $\sim 0.23r_{\text{vir}}$ ) seems to lie above the fitted curve as well. All regions except for Region C have similar entropy with cooling-flow cluster entropy profiles, where Regions A, B, and D lie below the fitted curve, and Regions E and F lie above.

The high entropy and the high temperature of Region E (the bridge) indicate a heating process that may be caused by the

gravitational pull of the ICM from subclusters that are at a pre-merger stage.

In addition to X-ray studies, the ICM of A3395 has been studied through the SZ effect with Planck. Planck Collaboration et al. (2013) report temperature and pressure values for the subclusters in A3395. Our Region D is enclosed in their A3395E region, and Region F is enclosed in the Planck A3395SW region. Their GNF2 pressure profile model results in  $kT = 5.0$  keV and  $P = 0.40 \times 10^{-2}$  keV cm $^{-3}$  for A3395E (Region D), and  $kT = 4.8$  keV and  $P = 0.40 \times 10^{-2}$  keV cm $^{-3}$  for A3395SW (Region F). With our NuSTAR analysis we find  $4.01^{+0.44}_{-0.37}$  and  $P = 0.33 \pm 0.04 \times 10^{-2}$  keV cm $^{-3}$  ( $5.35^{+0.68}_{-0.58} \times 10^{-12}$  dyn cm $^{-2}$ ) for Region D, and  $5.27^{+0.39}_{-0.34}$  keV and  $P = 0.48^{+0.04}_{-0.03} \times 10^{-2}$  keV cm $^{-3}$  ( $7.77^{+0.64}_{-0.57} \times 10^{-12}$  dyn cm $^{-2}$ ) for Region F. They do not report uncertainties for these specific regions (being model-dependent on global fits).

Although it is difficult to make a direct comparison between NuSTAR and Planck analyses since the derivation of pressure is based on different methods, it is important to state that our result reaches the Planck value within  $1\sigma$  errors. This is also a good validation of our scattered light treatment, as well as the assumptions used for the deprojection of thermodynamical maps, since the estimation of these parameters is the end product of multiple treatments, assumptions, and analyses.

We visually detected a point source in both NuSTAR and XMM-Newton images, and extracted a circular region with  $r = 1/2$  to study the source in detail from both NuSTAR and XMM-Newton data. We found that a powerlaw component with  $\Gamma = 1.48^{+0.56}_{-0.83}$  and a thermal plasma with  $kT = 1.81^{+0.95}_{-0.59}$  keV using NuSTAR data best describe the emission. For XMM-Newton analysis, we selected a region with the same area in the vicinity of this source due to the degeneracy of the powerlaw and *apec* components within the XMM-Newton bandpass. This analysis helped in estimating the plasma properties in the vicinity, and resulting parameters were adopted and fixed in the fit of the point-source region, which resulted in a powerlaw component with  $\Gamma = 1.86^{+0.10}_{-0.11}$ , which is better constrained than the NuSTAR photon index, since all *apec* parameters were frozen during the XMM-Newton fit. We also tried using an additional *apec* model instead of powerlaw, yet then the secondary *apec* temperature was around 5 keV, and the statistics were comparable, i.e.,  $C/\nu = 570.35/702$  for *apec* and  $C/\nu = 569.03/702$  for powerlaw. This  $\sim 5$  keV value is higher than what we find in Region C, where the point source resides, with NuSTAR, XMM-Newton, and Suzaku, as well as joint NuSTAR and XMM-Newton results, pointing to the degeneracy of a  $kT \sim 5$  keV thermal emission and  $\Gamma \sim 1.86$  power-law emission for the XMM-Newton analysis. Since NuSTAR covers a wider energy range, we claim that the true emission includes power-law emission as well as thermal emission within that region. The photon indices obtained from the two analyses agree within  $1\sigma$ , therefore we cannot claim a statistically significant variability between NuSTAR and XMM-Newton observations. When the XMM-Newton and NuSTAR spectra were simultaneously fit using a powerlaw + *apec* model, the *apec* component dominated the spectra, as expected due to the inclusion of more lower-energy XMM-Newton photons in the spectra.

In addition, results from NuSTAR spectral analysis for the temperature and the luminosity of the gas confined within this  $r = 1/2$  suggest that the point source may be a thermal corona embedded in a hot environment (Sun et al. 2007;

Tümer et al. 2019). The photon indices of  $\Gamma = 1.86^{+0.10}_{-0.11}$  for XMM-Newton and  $\Gamma = 1.48^{+0.56}_{-0.83}$  favor AGN emission rather than X-ray binaries ( $\Gamma \leq 1.4$ ) (see, e.g., Tozzi et al. 2006). Furthermore, the powerlaw component accounts for  $\sim 66\%$  of the total luminosity within 3.0–20.0 keV, and  $\sim 15\%$  within 0.5–2.0 keV based on NuSTAR analysis.

#### 4.4. On the Intercluster Filament

Guided by the literature (Tittley & Henriksen 2001; Lakhchaura et al. 2011; Planck Collaboration et al. 2013; Bourdin et al. 2020; Reiprich et al. 2021), we studied Regions A, B, and C in detail with the assumption that these regions may represent an interface of the A3395 ICM and the intercluster filament. Alvarez et al. (2018) find a global temperature of  $kT = 4.45^{+0.89}_{-0.55}$  keV and density  $n_e = 1.08^{+0.06}_{-0.05} \times 10^{-4}$  cm $^{-3}$  for the intercluster filament. The temperature results obtained from NuSTAR, XMM-Newton, Suzaku, and the joint NuSTAR and XMM-Newton spectral analysis of Regions A and B, are in agreement with Alvarez et al. (2018) for the filament within  $1\sigma$ . However, for Region C, the temperature results from NuSTAR analysis show a cooler plasma than what is found for the filament, yet this is in agreement within  $1.3\sigma$  with Alvarez et al. (2018) and within  $1\sigma$  with our XMM-Newton, Suzaku, and joint NuSTAR and XMM-Newton analyses. In addition, the density of the filament found by Sugawara et al. (2017) and Alvarez et al. (2018) is much smaller ( $\sim 1/4$ ) than the density we find for Regions A, B, and C.

The entropy is expected to rise to values higher than 1000 keV cm $^2$  outside  $0.5r_{200}$  (Pratt et al. 2006), due to heating by accretion shocks, and Lakhchaura et al. (2011) report high entropy and high temperature values for these regions. However, we do not observe such high entropy or temperature in Regions A, B, and C, which are expected to have higher entropy than the regions close to the center of the cluster (Piffaretti et al. 2005). In addition, the entropy we find for these regions is even lower than what is found at similar radii for cool-core clusters (Piffaretti et al. 2005).

These results, when studied in conjunction with the low temperature, low pressure, and high density values, suggest an excess of radiative cooling, which points to a flow of ICM into the filament, in contrast to Reiprich et al. (2021), who find high-temperature gas in the interface region and suggest heating by shocks via the ongoing merger activity. Such an offset cooling process is analogous to the more vigorous multiphase condensation “weather” occurring in dense cluster cores (Gaspari et al. 2018). Indeed, mergers drive a significant amount of turbulent motion, which can locally enhance density (Gaspari & Churazov 2013) and thus lead to localized enhanced filamentary cooling (Wittor & Gaspari 2020). Such detections of cooling in merger systems have become more frequent in recent years (e.g., Somboonpanyakul et al. 2021). Our results are also in line with Alvarez et al. (2018), who suggest that the ICM gas in the outskirts may be tidally moved into the filament during the interaction, as a part of the merging processes of A3395 and A3391. Such tidal motions can be seen as another form of large-scale turbulence, with the related eddies locally enhancing density.

## 5. Conclusion

We observed A3395 with NuSTAR for a total exposure time of  $\sim 125$  ks. We studied the northwestern region of the cluster



in conjunction with archival Suzaku and XMM-Newton observations. We find that the location of the cluster that meets the intercluster filament does not show any signs of heated plasma, but rather shows signs of excessive cooling. This is likely linked to the condensation “weather” enhanced by turbulence or tidal motions, in analogy to the core counterparts (e.g., Gaspari et al. 2020).

In addition, our temperature results from the NuSTAR data are in agreement with those from XMM-Newton and joint NuSTAR and XMM-Newton analysis for a region with  $\sim 25\%$  scattered light contamination within  $1\sigma$ , and we claim that temperature assessment of the intracluster medium is still valid even when the data are contaminated up to  $\sim 25\%$ . Our technique can be used for future NuSTAR observation proposals to estimate the possible scattered light contamination, and for its quantification during ICM analysis from moderately contaminated NuSTAR data.

We thank the anonymous referee for valuable discussions and suggestions that improved our work significantly. This research has made use of data from the NuSTAR mission, a project led by the California Institute of Technology, managed by the Jet Propulsion Laboratory (JPL), and funded by the National Aeronautics and Space Administration (NASA); XMM-Newton, an ESA science mission with instruments and contributions directly funded by ESA Member States and the

USA (NASA); and Suzaku satellite, a collaborative mission between the space agencies of Japan (JAXA) and the USA (NASA). In this work, we used the NuSTAR Data Analysis Software (NuSTARDAS) jointly developed by the ASI Science Data Center (ASDC, Italy) and the California Institute of Technology (USA). The data for this research have been obtained from the High Energy Astrophysics Science Archive Research Center (HEASARC), provided by NASA’s Goddard Space Flight Center. A.T. thanks Fiona A. Harrison, Kristin K. Madsen, and Brian W. Grefenstette for valuable discussions on scattered light, and Hervé Bourdin and Randall A. Rojas Bolivar for their contribution on the NuSTAR proposal process. A.T. and D.R.W. acknowledges support from NASA JPL RSA No.1657376 and from NASA ADAP award 80NSSC19K1443. M.G. acknowledges partial support by NASA Chandra GO8-19104X/GO9-20114X and HST GO-15890.020/023-A, and the *BlackHoleWeather* program. E.N.E. would like to thank Bogazici University BAP for financial support under the project No 13760.

## Appendix A NuSTAR Background Spectra

In this appendix, we present the NuSTAR background spectral fit in Figure 12. The background assessment is described in detail in Section 2.1 and in Wik et al. (2014).

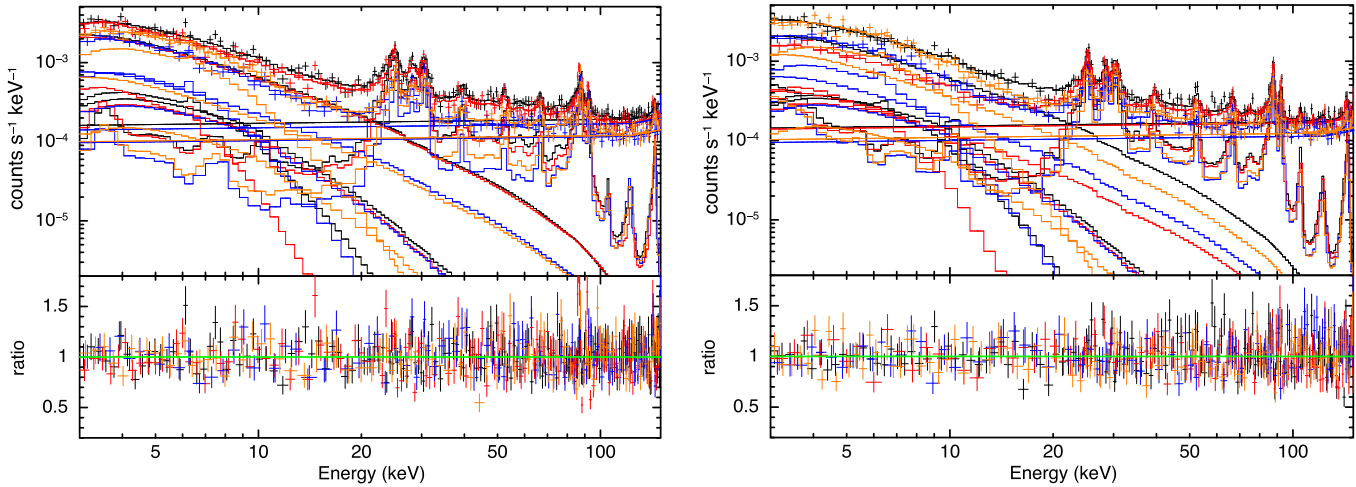


**Figure 12.** Joint fit of background and cluster emission of NuSTAR FPMA (left panel) and FPMB (right panel). Each color represents a region selected for the background fit.

## Appendix B

### Results of the Ray-trace Simulation Spectral Fits

In Figure 13 we present the spectral fits of the ray-traced single and double bounce photons extracted from regions of

interest shown in Figure 7. The fitting procedure is described in detail in Section 3.3.

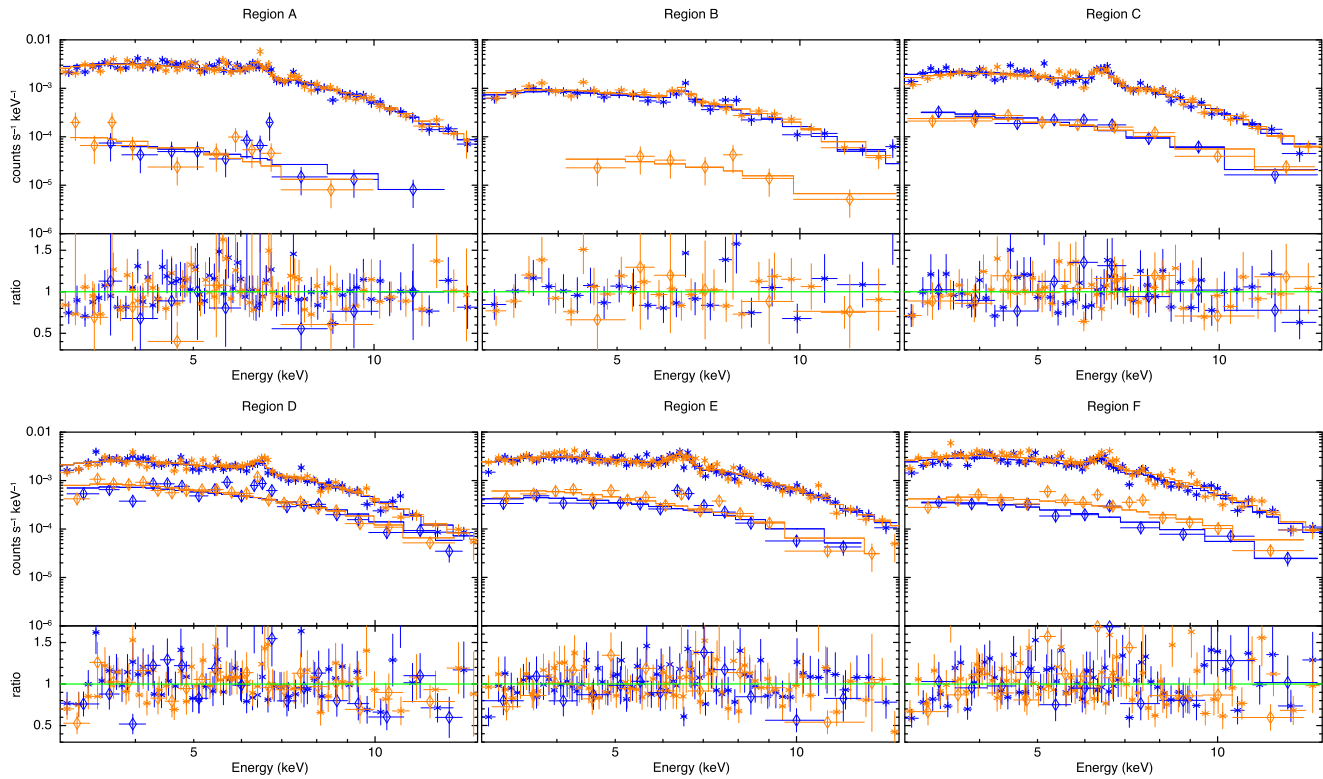


**Figure 13.** Ray-trace simulation fits of spectra from the regions of interest shown in Figure 7 in the 3–15 keV band, where blue denotes FPMA and orange denotes FPMB. Simulated singly reflected photons are presented with diamond markers, and simulated doubly reflected photons with asterisk markers. For plotting purposes, adjacent bins are grouped until they have a significant detection at least as large as  $5\sigma$ , with a maximum of five bins, except for the singly reflected photons in Regions A and B due to low counts. There were no data points from scattered light for FPMA for Region B between 3 and 15 keV, therefore it is not shown.

### Appendix C

#### Results of the Hot Spot Spectral Fits

The results of the spectral fit parameters from the circular region with  $r = 1'.5$ , centered at X shown in Figure 7, are presented in Table 6 for the XMM-Newton data and in Table 7 for the joint NuSTAR and XMM-Newton spectral analysis.

We realized different spectral fit processes by both freeing and fixing abundances and  $n_{\text{H}}$  values to give the fitting procedure more independence to find a high-temperature component. This analysis is described in detail in Section 3.4.

**Table 6**  
Spectral Parameters of XMM-Newton Analysis for the  $r = 1'.5$  Region Centered at X Shown in Figure 7 in the 0.5–9.0 keV Energy Band

	Fixed $n_{\text{H}}$		Free $n_{\text{H}}$	
	Fixed Z	Free Z	Fixed Z	Free Z
$n_{\text{H}}$ ( $10^{20} \text{ cm}^{-2}$ )	6.3	6.3	$8.51^{+2.92}_{-4.59}$	$11.0^{+20.1}_{-6.11}$
$kT$ (keV)	$4.79^{+1.88}_{-1.10}$	$5.13^{+1.80}_{-1.48}$	$4.43^{+2.15}_{-1.63}$	$3.98^{+2.44}_{-1.16}$
Z ( $Z_{\odot}$ )	0.23	$0.03^{+0.44}_{-0.03}$	0.23	$0.05^{+0.35}_{-0.05}$
$norm$ ( $10^{-5} \text{ cm}^{-5}$ )	$2.95^{+0.19}_{-0.21}$	$3.10^{+0.38}_{-0.23}$	$3.06^{+1.11}_{-0.36}$	$3.43^{+0.91}_{-0.60}$
$\chi^2/\nu$	181.39/97	180.27/96	180.52/96	179.13/95

**Note.** *apec* normalization ( $norm$ ) is given by  $\frac{10^{-14}}{4\pi[D_A(1+z)]^2} \int n_e n_{\text{H}} dV$ .



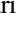
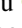
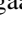


**Table 7**  
Spectral Parameters of NuSTAR (3.0–15.0 keV) and XMM-Newton (0.5–9.0 keV) Analysis for the  $r = 1'.5$  Region Centered at X Shown in Figure 7

	Fixed $n_{\text{H}}$		Free $n_{\text{H}}$	
	Fixed Z	Free Z	Fixed Z	Free Z
$n_{\text{H}}$ ( $10^{20} \text{ cm}^{-2}$ )	6.3	6.3	$14.8^{+18.1}_{-6.31}$	$13.7^{+7.71}_{-5.81}$
$kT$ (keV)	$3.75^{+0.72}_{-0.46}$	$3.97^{+0.55}_{-0.53}$	$3.58^{+0.55}_{-0.56}$	$3.74^{+0.56}_{-0.51}$
Z ( $Z_{\odot}$ )	0.23	0.09 (upper limit)	0.23	0.10 (upper limit)
$norm$ ( $10^{-5} \text{ cm}^{-5}$ )	$2.83^{+0.16}_{-0.29}$	$3.04^{+0.19}_{-0.26}$	$3.18^{+0.65}_{-0.36}$	$3.43^{+0.54}_{-0.42}$
$C/\nu$	1334.21/1200	1321.82/1199	1322.23/1199	1316.23/1198

**Note.** *apec* normalization ( $norm$ ) is given by  $\frac{10^{-14}}{4\pi[D_A(1+z)]^2} \int n_e n_{\text{H}} dV$ .



## ORCID iDs

Ayşegül Tümer  <https://orcid.org/0000-0002-3132-8776>  
 Daniel R. Wik  <https://orcid.org/0000-0001-9110-2245>  
 Massimo Gaspari  <https://orcid.org/0000-0003-2754-9258>  
 Hiroki Akamatsu  <https://orcid.org/0000-0003-1949-7005>  
 Niels J. Westergaard  <https://orcid.org/0000-0001-5839-8590>  
 Francesco Tombesi  <https://orcid.org/0000-0002-6562-8654>  
 E. Nihal Ercan  <https://orcid.org/0000-0003-0639-7048>

## References

- Akamatsu, H., Fujita, Y., Akahori, T., et al. 2017, *A&A*, **606**, A1  
 Alvarez, G. E., Randall, S. W., Bourdin, H., Jones, C., & Holley-Bockelmann, K. 2018, *ApJ*, **858**, 44  
 Anders, E., & Grevesse, N. 1989, *Geochim. Cosmochim. Acta*, **53**, 197  
 Arnaud, K. A. 1996, in ASP Conf. Ser. 101, *Astronomical Data Analysis Software and Systems V*, ed. G. H. Jacoby & J. Barnes (San Francisco, CA: ASP), 17  
 Bond, J. R., Kofman, L., & Pogosyan, D. 1996, *Natur*, **380**, 603  
 Bonjean, V., Aghanim, N., Salomé, P., Douspis, M., & Beelen, A. 2018, *A&A*, **609**, A49  
 Bourdin, H., Baldi, A. S., Kozmanyán, A., & Mazzotta, P. 2020, *EPJWC*, **228**, 00007  
 Cash, W. 1979, *ApJ*, **228**, 939  
 Cautun, M., van de Weygaert, R., Jones, B. J. T., & Frenk, C. S. 2014, *MNRAS*, **441**, 2923  
 Codis, S., Pichon, C., Devriendt, J., et al. 2012, *MNRAS*, **427**, 3320  
 De Grandi, S., Guzzo, L., Böhringer, H., et al. 1999, *ApJL*, **513**, L17  
 Donnelly, R. H., Forman, W., Jones, C., et al. 2001, *ApJ*, **562**, 254  
 Flin, P. 2003, *A&AT*, **22**, 841  
 Gaspari, M. 2015, *MNRAS*, **451**, L60  
 Gaspari, M., Brighenti, F., Temi, P., & Etori, S. 2014, *ApJL*, **783**, L10  
 Gaspari, M., & Churazov, E. 2013, *A&A*, **559**, A78  
 Gaspari, M., Eckert, D., Etori, S., et al. 2019, *ApJ*, **884**, 169  
 Gaspari, M., McDonald, M., Hamer, S. L., et al. 2018, *ApJ*, **854**, 167  
 Gaspari, M., Tombesi, F., & Cappi, M. 2020, *NatAs*, **4**, 10  
 Gastaldello, F., Wik, D. R., Molendi, S., et al. 2015, *ApJ*, **800**, 139  
 Gitti, M., O'Sullivan, E., Giacintucci, S., et al. 2010, *ApJ*, **714**, 758  
 Hahn, O., Porciani, C., Carollo, C. M., & Dekel, A. 2007, *MNRAS*, **375**, 489  
 Harrison, F. A., Craig, W. W., Christensen, F. E., et al. 2013, *ApJ*, **770**, 103  
 Henry, J. P., & Briel, U. G. 1995, *ApJL*, **443**, L9  
 Hincks, A. D., Radiconi, F., Romero, C., et al. 2022, *MNRAS*, **510**, 3335  
 Ishisaki, Y., Maeda, Y., Fujimoto, R., et al. 2007, *PASJ*, **59**, 113  
 Jones, D. H., Read, M. A., Saunders, W., et al. 2009, *MNRAS*, **399**, 683  
 Kalberla, P. M. W., Burton, W. B., Hartmann, D., et al. 2005, *A&A*, **440**, 775  
 Koyama, K., Tsunemi, H., Dotani, T., et al. 2007, *PASJ*, **59**, 23  
 Kraljic, K., Arnouts, S., Pichon, C., et al. 2018, *MNRAS*, **474**, 547  
 Kuchner, U., Aragón-Salamanca, A., Pearce, F. R., et al. 2020, *MNRAS*, **494**, 5473  
 Kull, A., & Böhringer, H. 1999, *A&A*, **341**, 23  
 Laigle, C., Pichon, C., Codis, S., et al. 2015, *MNRAS*, **446**, 2744  
 Lakhchaura, K., Singh, K. P., Saikia, D. J., & Hunstead, R. W. 2011, *ApJ*, **743**, 78  
 Lidders, K., Palme, H., & Gail, H. P. 2009, *LanB*, **4B**, 712  
 Lovisari, L., Etori, S., Gaspari, M., & Giles, P. A. 2021, *Univ*, **7**, 139  
 Madsen, K. K., Christensen, F. E., Craig, W. W., et al. 2017, *JATIS*, **3**, 044003  
 Markevitch, M., Forman, W. R., Sarazin, C. L., & Vikhlinin, A. 1998, *ApJ*, **503**, 77  
 Markevitch, M., Sarazin, C. L., & Vikhlinin, A. 1999, *ApJ*, **521**, 526  
 Markevitch, M., & Vikhlinin, A. 2007, *PhR*, **443**, 1  
 Marziani, P., D'Onofrio, M., Bettoni, D., et al. 2017, *A&A*, **599**, A83  
 Mitsuda, K., Jetzer, P., Kaastra, J. S., & Tamura, T. 2005, *PASJ*, **59**, 1  
 Munro, D. H., & Dubois, P. F. 1995, *ComPh*, **9**, 609  
 Nakamura, F. E., Hattori, M., & Mineshige, S. 1995, *A&A*, **302**, 649  
 Paturel, G., Petit, C., Prugniel, P., et al. 2003, *A&A*, **412**, 45  
 Piffaretti, R., Jetzer, P., Kaastra, J. S., & Tamura, T. 2005, *A&A*, **433**, 101  
 Planck Collaboration, Ade, P. A. R., Aghanim, N., et al. 2013, *A&A*, **550**, A134  
 Pratt, G. W., Arnaud, M., & Pointecouteau, E. 2006, *A&A*, **446**, 429  
 Reiprich, T. H., Veronica, A., Pacaud, F., et al. 2021, *A&A*, **647**, A2  
 Rossetti, M., Ghizzardi, S., Molendi, S., & Finoguenov, A. 2007, *A&A*, **463**, 839  
 Sarazin, C. L. 1986, *RvMP*, **58**, 1  
 Schellenberger, G., Reiprich, T. H., Lovisari, L., Nevalainen, J., & David, L. 2015, *A&A*, **575**, A30  
 Smith, R. K., Brickhouse, N. S., Liedahl, D. A., & Raymond, J. C. 2001, *ApJL*, **556**, L91  
 Somboonpanyakul, T., McDonald, M., Bayliss, M., et al. 2021, *ApJL*, **907**, L12  
 Strüder, L., Briel, U., Dennerl, K., et al. 2001, *A&A*, **365**, L18  
 Sugawara, Y., Takizawa, M., Itahana, M., et al. 2017, *PASJ*, **69**, 93  
 Sun, M., Jones, C., Forman, W., et al. 2007, *ApJ*, **657**, 197  
 Tawa, N., Hayashida, K., Nagai, M., et al. 2008, *PASJ*, **60**, 11  
 Tittley, E. R., & Henriksen, M. 2001, *ApJ*, **563**, 673  
 Tozzi, P., Gilli, R., Mainieri, V., et al. 2006, *A&A*, **451**, 457  
 Tümer, A., Tombesi, F., Bourdin, H., et al. 2019, *A&A*, **629**, A82  
 Turner, M. J. L., Abbey, A., Arnaud, M., et al. 2001, *A&A*, **365**, L27  
 Valageas, P., Schaeffer, R., & Silk, J. 2003, *MNRAS*, **344**, 53  
 Voit, G. M., Kay, S. T., & Bryan, G. L. 2005, *MNRAS*, **364**, 909  
 Werner, N., Finoguenov, A., Kaastra, J. S., et al. 2008, *A&A*, **482**, L29  
 Westergaard, N. J. 2011, *Proc. SPIE*, **8147**, 81470Y  
 Wik, D. R., Hornstrup, A., Molendi, S., et al. 2014, *ApJ*, **792**, 48  
 Wilms, J., Allen, A., & McCray, R. 2000, *ApJ*, **542**, 914  
 Wittor, D., & Gaspari, M. 2020, *MNRAS*, **498**, 4983  
 Zinger, E., Dekel, A., Birnboim, Y., Kravtsov, A., & Nagai, D. 2016, *MNRAS*, **461**, 412